Structure, Function, and Evolution of the Pseudomonas aeruginosa Lysine Decarboxylase LdcA

Eaazhisai Kandiah, Diego Carriel, Pierre Simon Garcia, Jan Felix, Manuel Banzhaf, George Kritikos, Maria Bacia-Verloop, Céline Brochier-Armanet, Sylvie Elsen, Irina Gutsche

Article

Structure

Structure, Function, and Evolution of the *Pseudomonas aeruginosa* Lysine Decarboxylase LdcA

Graphical Abstract

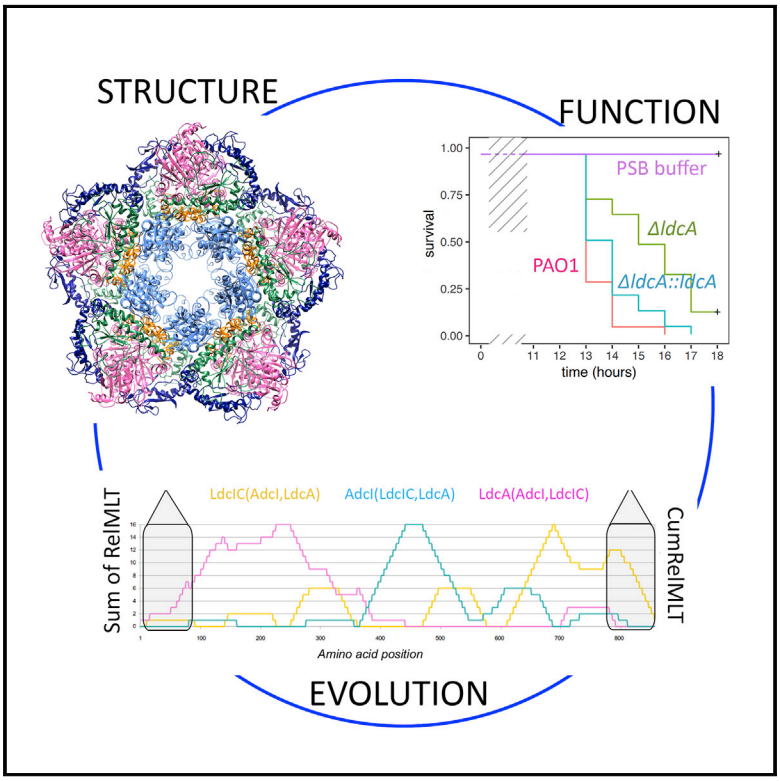

Highlights

- The structure of the *P. aeruginosa* LdcA is solved to 3.7-Å resolution by cryo-EM
- The phylogenetic signal shifts within structural/functional domains of LAdcs
- LdcA is involved in *P. aeruginosa* physiology and full virulence
- *P. aeruginosa ravAviaA* operon has a potentially defensive function

Authors

Eaazhisai Kandiah, Diego Carriel, Pierre Simon Garcia, ..., Céline Brochier-Armanet, Sylvie Elsen, Irina Gutsche

Correspondence

irina.gutsche@ibs.fr

In Brief

Kandiah et al. solve the structure of the lysine decarboxylase LdcA from a human pathogen *Pseudomonas aeruginosa* by cryo-EM. They use evolutionary information to analyze the system, demonstrate involvement of LdcA in full virulence of the pathogen *in vivo*, and propose to target this protein for therapeutic interventions.

Kandiah et al., 2019, Structure *27*, 1–13
December 3, 2019
https://doi.org/10.1016/j.str.2019.10.003

CellPress

Please cite this article in press as: Kandiah et al., Structure, Function, and Evolution of the *Pseudomonas aeruginosa* Lysine Decarboxylase LdcA, Structure (2019), https://doi.org/10.1016/j.str.2019.10.003

Structure
Article

CellPress

Structure, Function, and Evolution of the *Pseudomonas aeruginosa* Lysine Decarboxylase LdcA

Eaazhisai Kandiah,[1,6] Diego Carriel,[1,2] Pierre Simon Garcia,[3,4] Jan Felix,[1] Manuel Banzhaf,[5] George Kritikos,[5] Maria Bacia-Verloop,[1] Céline Brochier-Armanet,[3,4] Sylvie Elsen,[2] and Irina Gutsche[1,7,*]
[1]Univ. Grenoble Alpes, CNRS, CEA, CNRS, Institut de Biologie Structurale (IBS), 38000 Grenoble, France
[2]Biology of Cancer and Infection, U1036 INSERM, CEA, University of Grenoble Alpes, ERL5261 CNRS, Grenoble, France
[3]Univ Lyon, Université Lyon 1, CNRS, UMR5558, Laboratoire de Biométrie et Biologie Évolutive, 43 bd du 11 novembre 1918, 69622 Villeurbanne, France
[4]MMSB Molecular Microbiology and Structural Biochemistry, Institut de Biologie et de Chimie des Protéines 7 Passage du Vercors, 69367 Lyon Cedex 07, France
[5]Institute of Microbiology & Infection and School of Biosciences, University of Birmingham, Edgbaston, B15 2TT Birmingham, UK
[6]Present address: European Synchrotron Radiation Facility, 71 Ave des Martyrs, 38000 Grenoble, France
[7]Lead Contact
*Correspondence: irina.gutsche@ibs.fr
https://doi.org/10.1016/j.str.2019.10.003

SUMMARY

The only enzyme responsible for cadaverine production in the major multidrug-resistant human pathogen *Pseudomonas aeruginosa* is the lysine decarboxylase LdcA. This enzyme modulates the general polyamine homeostasis, promotes growth, and reduces bacterial persistence during carbenicillin treatment. Here we present a 3.7-Å resolution cryoelectron microscopy structure of LdcA. We introduce an original approach correlating phylogenetic signal with structural information and reveal possible recombination among LdcA and arginine decarboxylase subfamilies within structural domain boundaries. We show that LdcA is involved in full virulence in an insect pathogenesis model. Furthermore, unlike its enterobacterial counterparts, LdcA is regulated neither by the stringent response alarmone ppGpp nor by the AAA+ ATPase RavA. Instead, the *P. aeruginosa ravA* gene seems to play a defensive role. Altogether, our study identifies LdcA as an important player in *P. aeruginosa* physiology and virulence and as a potential drug target.

INTRODUCTION

Amino acid decarboxylases are ubiquitous enzymes involved in physiologically important processes ranging from the synthesis of polyamines to bacterial survival during acid stress response. Bacterial AAT-fold basic amino acid decarboxylases are pyridoxal 5′-phosphate (PLP)-dependent enzymes termed LAO decarboxylases, or LAOdc, because they decarboxylate lysine (LdcI and LdcC), arginine (AdcI), and ornithine (OdcI and OdcC) into corresponding polyamine products; the suffixes "I" and "C" denote the acid stress inducible and the constitutive (i.e., biosynthetic) subfamily, respectively (Kanjee and Houry, 2013). The most prevalent diamine, putrescine, can be made directly from ornithine by an Odc (Orn → Put) or indirectly from arginine via agmatine by an Adc (Arg → Agm), whereas Ldc transforms lysine into cadaverine (Lys → Cad), widespread in particular in Proteobacteria. These enzymatic reactions are associated with proton consumption and release of CO_2 and the polyamine, and therefore contribute to buffering the cytosol in acid stress response, while the primary function of the acid stress-unrelated biosynthetic LAOdcs is polyamine production (Kanjee and Houry, 2013). Indeed, as polycations, polyamines are capable of binding negatively charged macromolecules such as nucleic acids, membrane phospholipids, and proteins, and therefore are involved in primordial processes as diverse as DNA replication, gene expression, protein synthesis, stress and antibiotic resistance, siderophore synthesis, biofilm formation, and virulence (Michael, 2016b, 2016a).

Pseudomonas aeruginosa is a major opportunistic human pathogen causing severe diseases that can be life threatening in patients with compromised host defense mechanisms (Moradali et al., 2017; Winstanley et al., 2016). Exhaustive phylogenetic analysis of prokaryotic AAT-fold LAOdcs (Carriel et al., 2018) revealed that proteobacterial LAOdcs are divided into two monophyletic groups, Odc and LAdc (Carriel et al., 2018), and that LAdc can be further subdivided into three subfamilies–LdcA, LdcIC, and AdcI—the latter being seemingly spread mainly through horizontal gene transfer (HGT). The previously unidentified LdcA subfamily, ancestral in two unrelated taxa, *Betaproteobacteria* and *Pseudomonadaceae* (*Gammaproteobacteria*), is evolutionary distinct from the LdcIC subfamily, which is composed of LdcI, ancestral in some *Gammaproteobacteria* families (including *Enterobacteriaceae*) and in *Francisellaceae*, and LdcC, which emerged from a gene duplication of *ldcI* (Carriel et al., 2018). *P. aeruginosa* LdcA, the only Cad-producing enzyme in *P. aeruginosa* PAO1 (Carriel et al., 2018), was actually predicted to be an AdcI since the promoter of the corresponding gene *PA1818* in the PAO1 strain is

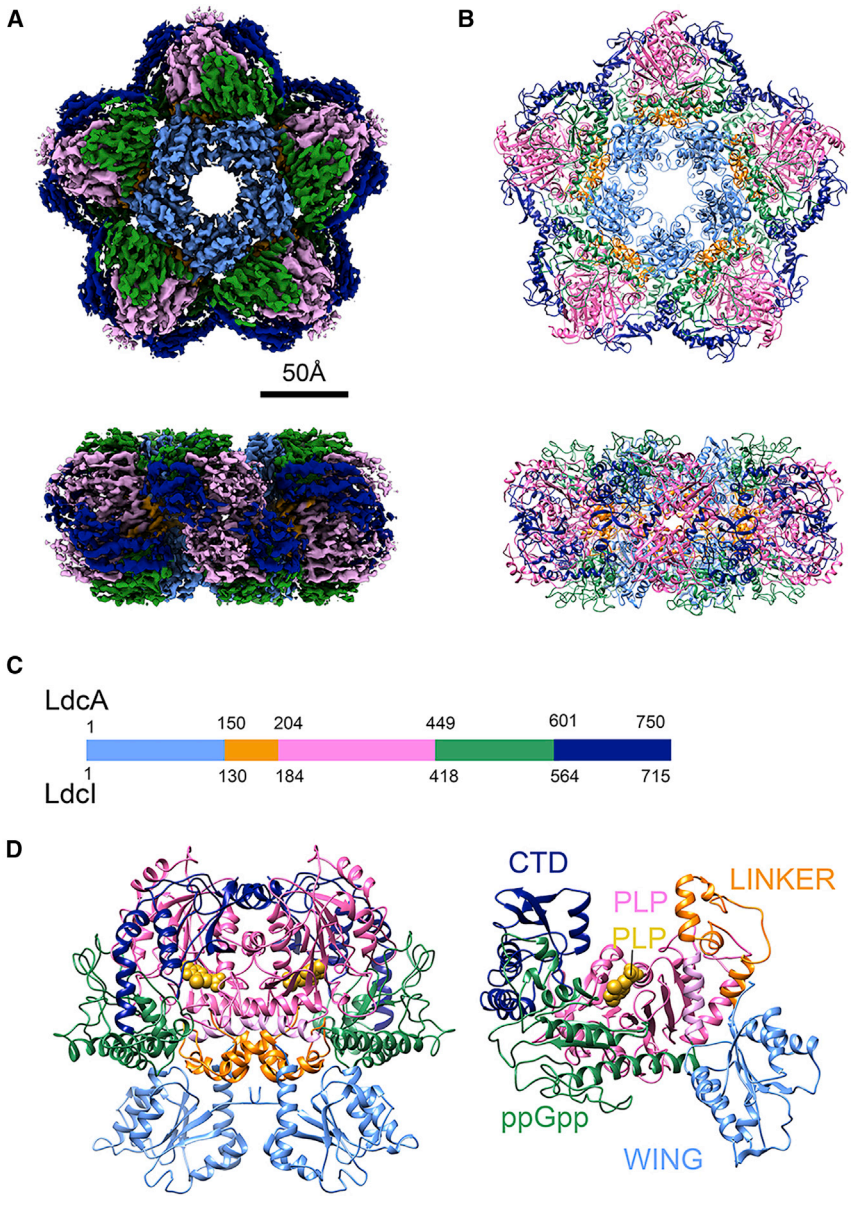

Figure 1. Cryo-EM Map and Near-Atomic Model of LdcA

(A and B) Top and side views of the LdcA map (A) and the atomic model (B), colored according to domains. The wing domain is shown in blue, linker in orange, PLP in pink, ppGpp in green and CTD in marine.

(C) Schematic representation of the LdcA sequence colored as above. Amino acid residue numbers of LdcA are marked above and corresponding residue numbers of LdcI below.

(D) Cartoon representation of the monomer and dimer atomic models colored according to domains.

induced by arginine via the arginine-responsive regulator ArgR (Chou et al., 2010; Lu et al., 2004). Yet, the *PA1818* gene was shown to be essential for *P. aeruginosa* lysine utilization, and the purified protein was found to possess an Ldc activity at slightly basic pH (Chou et al., 2010).

Despite in-depth phylogenetic analysis, relationships between the LdcA subfamily and LdcIC and AdcI subfamilies remained unresolved (Carriel et al., 2018). Thus, because high-resolution crystal structures of *Escherichia coli* LdcI (Kanjee et al., 2011a) and AdcI (Andréll et al., 2009) are known (Figure S1), in the present work we address the structure-function relationships of LAdcs in relation to their evolutionary history by determining the cryoelectron microscopy (cryo-EM) structure of *P. aeruginosa* LdcA and by developing an original approach combining phylogenetic and structural information. Considering effects of LdcA on the pathogen growth, persistence, and global polyamine homeostasis (Carriel et al., 2018), and taking into account severe pleiotropic effects of polyamines on bacterial physiology and their notorious link to virulence (Michael, 2016a, 2016b), we examine the influence of *ldcA* inactivation on *P. aeruginosa* virulence in *Galleria* larvae of the greater wax moth, which is a robust model to evaluate virulence of Gram-negative bacteria (Ramarao et al., 2012; Tsai et al., 2016). Furthermore, we structurally and biochemically demonstrate and explain why, opposite to LdcIC (Kanjee et al., 2011a) but similarly to AdcI (Kanjee et al., 2011b), LdcA activity is not inhibited by the alarmone of the stringent response ppGpp. Finally, we examine potential relationships between *P. aeruginosa* LdcA and a MoxR AAA+ ATPase RavA, whose enterobacterial homolog was shown to protect LdcI from ppGpp inhibition thereby enabling *E. coli* to simultaneously sustain acid and nutrient stresses (El Bakkouri et al., 2010; Kanjee et al., 2011a; Malet et al., 2014; Snider et al., 2006). Taken together, this study identifies LdcA as an important player in *P. aeruginosa* virulence through its involvement in polyamine metabolism and hence as a potential drug target.

RESULTS

Structural Characterization of *P. aeruginosa* LdcA by Cryo-EM

The structure of *P. aeruginosa* LdcA was solved by single-particle cryo-EM at an overall resolution of 3.7 Å (Figure 1, S1, and S2; Table S1). The map showcases a D5-symmetrical decamer, or pentamer of dimers, arranged around a central channel (Figure 1). The global shape and ~200-Å diameter of the LdcA double-ring with a ~20-Å hole are very similar to the previously solved structures of LdcI (PDB: 3N75; Kanjee et al., 2011a), LdcC (PDB: 5FKZ; and EMDB 3205; Kandiah et al., 2016), and AdcI (PDB: 2VYC; Andréll et al., 2009) of *E. coli*, but differ from

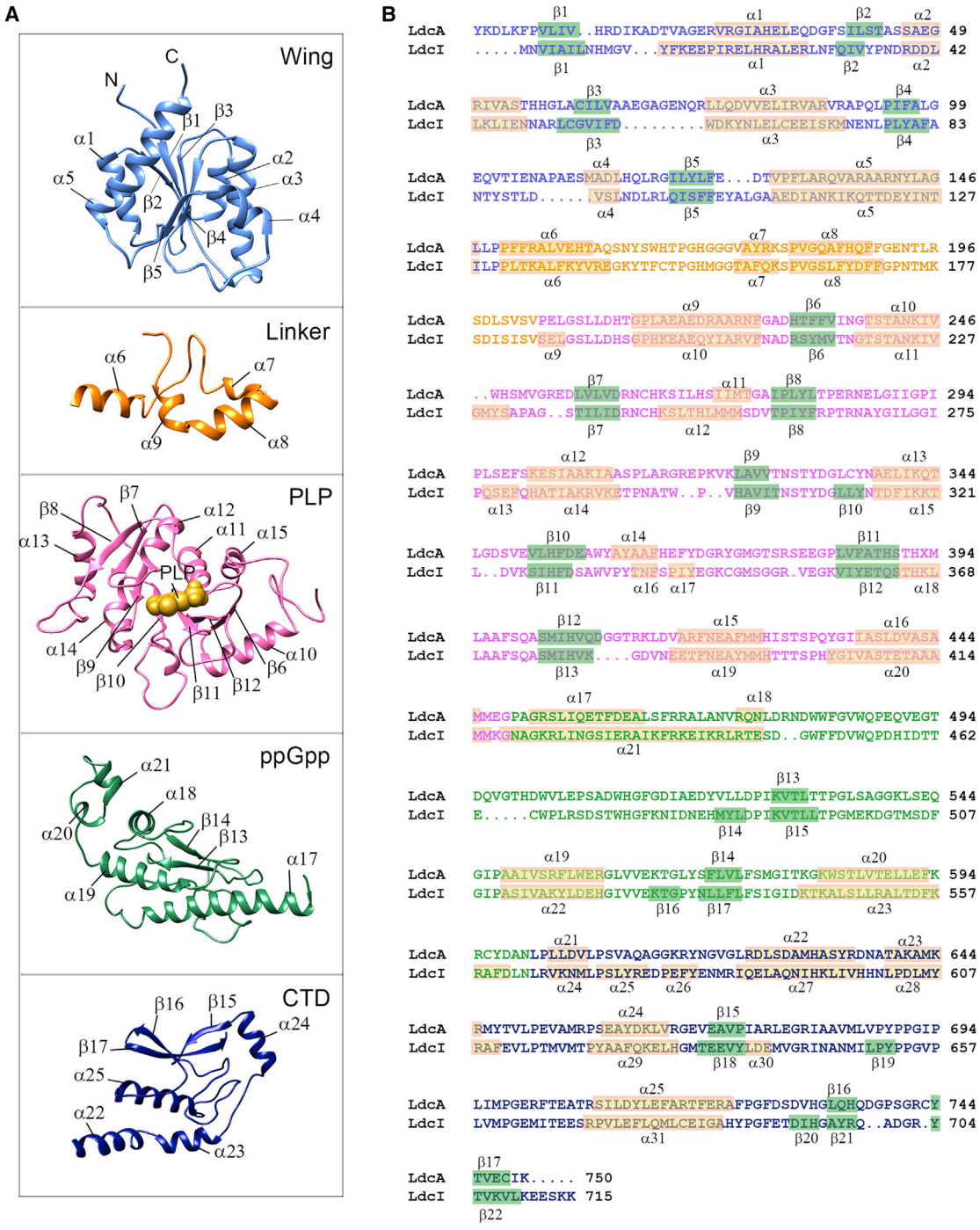

Figure 2. Domain Folds, Sequence, and Structural Elements of LdcA and LdcI

(A) Individual domain folds.

(B) Sequence alignment of *P. aeruginosa* LdcA and *E. coli* LdcI, amino acids colored according to domains, secondary structure elements indicated for both sequences and numbered accordingly.

the dodecameric *Lactobacillus saerimneri 30a* OdcI (PDB: 1ORD; Momany et al., 1995), acquired from an enterobacterium by HGT. The LdcA monomer (residues 1–750) can be divided into three structural domains annotated as in other LAOdcs (Figures 1 and 2): the N-terminal wing domain (residues 1–149), the central core domain (residues 150–600) and the peripheral C-terminal domain (CTD) (residues 601–750). The core domain is composed of a small linker domain (residues 150–203), a PLP-binding domain (residues 204–448) and an AAT-like small domain (residues 449–600). In LdcI and LdcC, the latter can be

referred to as the ppGpp-binding domain because of its strong interaction with the stringent response alarmone ppGpp, resulting in a complete inhibition of the lysine decarboxylase activity of these enzymes (Kanjee et al., 2011a, 2011b). AdcI, however, is not inhibited by ppGpp, despite conservation of the ppGpp-binding residues (Kanjee et al., 2011b). Corresponding numbering for LdcI is indicated in Figures 1C and 2.

In decameric LdcA, two monomers form a C2-symmetric dimer, which represents the basic unit of the structure (Figure 1D) and forms a decameric assembly through strong inter-ring contacts between adjacent dimers. This type of dimerization is typical for proteobacterial LAOdcs and for PLP-dependent enzymes in general, and leads to a completion of the active sites of each monomer buried into a cleft at the dimer interface. The dimer is mainly maintained by a tight association of the core domains of each monomer, whereas the wing domains protrude into the central pore of the double-toroid, being primarily responsible for interactions that stabilize the ring assembly from the dimeric building blocks. Finally, the CTDs line the periphery of the double-toroid (Figure 1A), contributing to the creation of a deep channel leading to the PLP-binding active site located 30 Å away from the enzyme surface.

The multimeric and multidomain nature of the proteobacterial AAT-fold LAOdcs hampers straightforward comparison of the atomic model of the *P. aeruginosa* LdcA decamer with those of the *E. coli* LdcI and AdcI decamers, and of the *L. saerimneri 30a* OdcI dodecamer. Calculation of root-mean-square deviation (RMSD) between the entire assemblies or between extracted dimers, as well as between monomers or between each of the individual domains subjected to rigid body fit, could not provide sufficient insights apart from confirming a general impression that LdcA seemed more similar to AdcI than to LdcI or OdcI (Table S2). Therefore, we opted for an original approach that combines structural information with phylogenetic signals characteristic of different LAOdc subfamilies.

Sliding Window Phylogenetic Analysis Suggests Recombination Events within Structural Domains of LAdcs

Previous phylogenetic analysis of proteobacterial LAOdcs unambiguously revealed OdcIC as the first diverging subfamily, while the relationships among the LAdc subfamilies remained unresolved despite the use of accurate evolutionary models and tree reconstruction procedures (Carriel et al., 2018). A phylogenetic maximum likelihood (ML) analysis using OdcIC as an outgroup, resulted in AdcI and LdcA grouped together, to the exclusion of LdcIC (Figure S1). However, the branch separating LdcIC from LdcA and AdcI was very short and associated to a moderate bootstrap value (BV = 66%, Figure S1), meaning that this branch was weakly supported by the information contained in sequences. This could be due either to a global lack of phylogenetic signal in the sequences or to the presence of conflicting phylogenetic signals. The lack of phylogenetic signal may be explained by one of the following hypotheses (Gribaldo and Brochier, 2009). First, multiple substitutions may have progressively erased the most ancient phylogenetic signals contained in sequences. Second, too few substitutions may have occurred during the divergence of the three subfamilies, possibly because they diverged in a short time period. Alternatively, conflicting phylogenetic signals could result from recombination events among subfamilies.

To discriminate between these hypotheses, we analyzed the phylogenetic signal contained in LAOdc sequences using a sliding window (Figure 3). Under the assumption of a lack of phylogenetic signal, inferred trees are expected to be mostly unresolved, while resolved but inconsistent trees are expected if conflicting phylogenetic signals are contained in the alignment. As expected, BVs associated to the 157 ML trees obtained using an 80-amino acid long window sliding with a step of 5 were relatively moderate. Nevertheless, clear tendencies emerged, indicating that LAOdc sequences do contain phylogenetic signal. The consistency of the 157 ML trees was evaluated with SplitTree (Huson and Bryant, 2006). The resulting phylogenetic network strongly supported the OdcIC subfamily as monophyletic and clearly separated from the three other subfamilies (Figure S3). Similarly, LdcIC appeared monophyletic and well distinct from other subfamilies. This indicated that the monophyly of OdcIC on the one hand and of LdcIC on the other was recovered in most ML trees. In contrast, reticulated splits could be observed at the base of AdcI and of LdcA, showing that the monophyly of these subfamilies was less frequently recovered (Figure S3).

We next computed several scores describing the monophyly of LAOdc subfamilies and their relationships along the multiple alignment. More precisely, the monophyly of each LAOdc subfamily was described by two scores: the Subfamily Maximum Likelihood Tree score (SubMLT) and Subfamily Bootstrap Replicate Trees score (SubBRT) (see the STAR Methods). The three possible relationships among LdcA, LdcIC, and AdcI—namely (1) the grouping of LdcA and LdcIC, to the exclusion of AdcI (i.e., AdcI(LdcIC, LdcA)), (2) the sistership between LdcA and AdcI (i.e., LdcIC(LdcA, AdcI)), and (3) the clustering of LdcIC and AdcI (i.e., LdcA(LdcIC, AdcI))—were described by the Relationship Maximum Likelihood Tree (RelMLT), the Relationship Bootstrap Replicates Tree scores (RelBRT), and the Cumulative Relationship Maximum Likelihood Tree score (CumRelMLT). These scores were calculated for each sliding window and mapped on the alignment. In agreement with the phylogenetic network, the monophyly of OdcIC and LdcIC subfamilies was recovered all along the alignment and strongly supported by SubMLT and SubBRT scores (SubMLT = 1 and SubBRT scores >80%, Figure 3). The monophyly of the LdcA subfamily was mainly observed in trees corresponding to the C-terminal half of sequences (SubMLT = 1), albeit with moderate-to-low SubBRT scores. Specifically, in trees corresponding to the N-terminal region, sequences from *Pseudomonas* do not group with *Betaproteobacteria* sequences. In contrast, the monophyly of AdcI was observed only in 80 ML trees (51%), as illustrated by the discontinuous SubMLT scores and the overall low SubBRT scores (Figure 3). Altogether, these results were consistent with the picture provided by the phylogenetic network (Figure S3), and confirmed that sequences contained a clear phylogenetic signal for the monophyly of LdcIC and OdcIC. In this context, the absence of support for the monophyly of LdcA and AdcI suggested recombination events between members of these two families.

Regarding relationships among subfamilies, our approach disclosed a puzzling picture, with the three topologies being

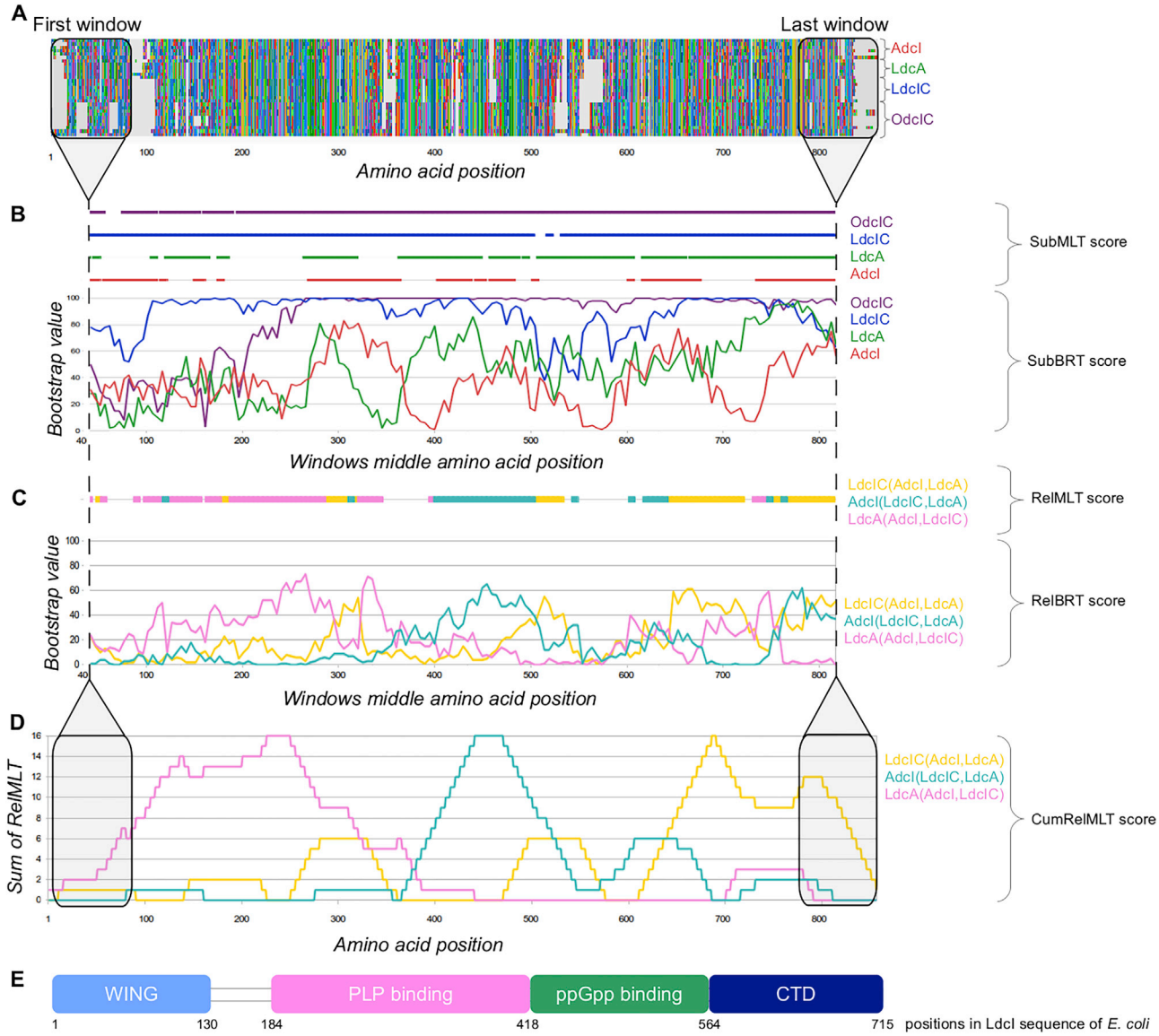

Figure 3. Sliding Window Analysis

(A) Multiple alignment of 32 LAOdc sequences.

(B) Subfamily ML/BR tree scores for OdcIC, LdcIC, LdcA, and AdcI associated to each 80-amino acid window.

(C) Relationship ML/BR trees score for the three possible relationships among the four subfamilies.

(D) Cumulative relationship ML tree score of the three possible relationships among the four subfamilies.

(E) Domain composition of *E. coli* LdcI. The first and last windows are represented in gray rounded rectangles.

supported by different regions of the alignment (Figure 3). This observation was compatible with the hypothesis of a mixture of phylogenetic signals contained in the sequences. The region encompassing the wing domain and the first half of the PLP-binding domain positioned LdcA as the first diverging subfamily, while LdcIC and AdcI appeared more closely related (i.e., LdcA(AdcI, LdcIC)), albeit with moderate supports (low RelBRT and CumMLT scores, Figure 3). In contrast, the second half of the PLP-binding domain and the beginning of the ppGpp-binding domain supported a close relationship between LdcA and LdcIC, to the exclusion of AdcI (i.e., AdcI(LdcIC, LdcA)), again with moderate RelBRT and CumMLT scores. The phylogenetic signal contained in the central part of the ppGpp-binding domain was very low and did not support any topology (RelMLT = 0, RelBRT <40%, and CumRelBRT <7; Figure 3). Finally, the C-terminal part of the ppGpp-binding domain and the CTD contained a mixture of signals with a preference for the topology separating LdcIC from AdcI and LdcA (i.e., LdcIC(LdcA, AdcI)) (Figure 3).

Taken together, while the sliding window approach did not entirely disclose the relationships among the LAOdc subfamilies, it clearly demonstrated that, in the case of LAdcs, the nature of the phylogenetic signal varies according to the considered region of the proteins. This result is consistent with the hypothesis of recombination events among subfamilies. Importantly, the

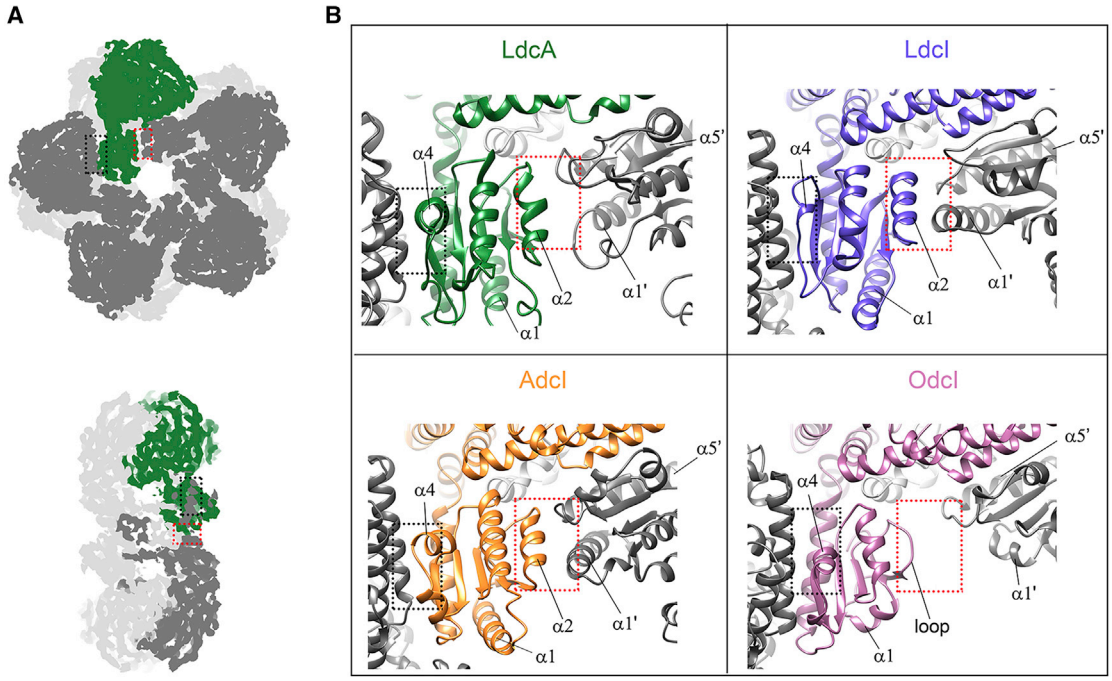

Figure 4. Wing Domain Contacts in LdcA, LdcI, AdcI, and OdcI

(A) Surface representation of the top and side views of the LdcA decamer, with one monomer shown in green, the other monomers of the top ring in dark gray and those of the bottom ring in light gray. Inside each ring, monomers make wing-wing (red rectangle) and wing-core contacts (black rectangle).

(B) Comparison of these contacts in LdcA (green), LdcI (blue), AdcI (orange), and OdcI (pink) atomic models. Secondary structure elements from a neighboring monomer are indicated by a single quote (').

three different phylogenetic signals do not match the boundaries of the structural domains, meaning that, if they resulted from recombination events, these occurred within domains (Figures 2 and 3). Accordingly, a simple domain-wise structural alignment would not bring meaningful insights. However, as shown below, the phylogenetic signals can be ingeniously used in structural comparison. In particular, the CumRelMLT values can be mapped on the 3D structure using a color gradient to correlate phylogenetic signal with structural information (Figure 5; Table S3).

P. aeruginosa LdcA Has Decreased Interactions between Wing Domains, a Feature Shared with OdcI despite the Decameric Assembly of LdcA

The wing domain of *P. aeruginosa* LdcA adopts a so-called REC domain fold, wherein a five-stranded parallel β sheet (β2-β1-β3-β4-β5) is sandwiched between two sets of amphipathic helices, three (α2, α3, and α4) facing one side of the sheet and an additional two (α1 and α5) on the other side (Figure 2A). This arrangement is analogous to LdcI (Kanjee et al., 2011a), while AdcI has an additional short helix located at the C-terminal edge of the sheet (Andréll et al., 2009). Although the overall fold of the wing domain is similar to previously solved LAOdc structures (Table S2), several specificities of the α helices of the LdcA wing domain should be explicitly mentioned (Figure 4). One of the notable particularities is the orientation of the α1 helix in a way that the extended loop after this helix is projected more inward toward the center of the decamer. This gives an impression that the central pore of LdcA (less than ~20 Å in diameter) is smaller than in AdcI and LdcI where the pore diameter is ~25 Å. Furthermore, the wing domain of each LdcA monomer is involved in two sets of interactions with the adjacent monomer of the same ring, one via wing-wing contacts and second via wing-core contacts (Figure 4). Importantly, in comparison with the LdcI and the AdcI decamer structures, in the LdcA decamer the wing-wing interaction is considerably weakened due to a massive reorientation of helices α1 and α5 relative to α2. Yet, these three helices are described as the wing interlocking system required for the decameric assembly of lysine and arginine decarboxylases (Andréll et al., 2009; Kanjee et al., 2011a). In particular α1 of LdcA is almost two turns shorter (~10 Å) than that of LdcI, thereby precluding its interaction with the α2 of the neighboring monomer in the ring, reminiscent of the *L. saerimneri 30a* OdcI structure. In OdcI, the α2 helix is replaced by a loop resulting in a loss of this interaction (Figure 4), which is proposed to be an explanation of the dodecameric instead of decameric assembly of this enzyme (Kanjee et al., 2011a; Momany et al., 1995). The inferred decreased wing-wing interaction is consistent with the lesser buried surface area between two successive protomers in an LdcA and OdcI ring compared with an LdcI or AdcI ring (Table S4). Finally, the orientation of the LdcA helices α3 and α4, not involved in the inter-wing contacts, also differs from the other decarboxylases. Notably, the C-terminal edge of the α4 in LdcI is involved in ppGpp binding. The similarity in wing-wing contacts observed between LdcA and OdcIC on the one hand, and between LdcIC and AdcI on the other, is consistent with the phylogenetic signal contained in sequences supporting a close relationship between LdcIC and AdcI, to the exclusion of LdcA, at the level of the wing domains (Figure 3). This observation

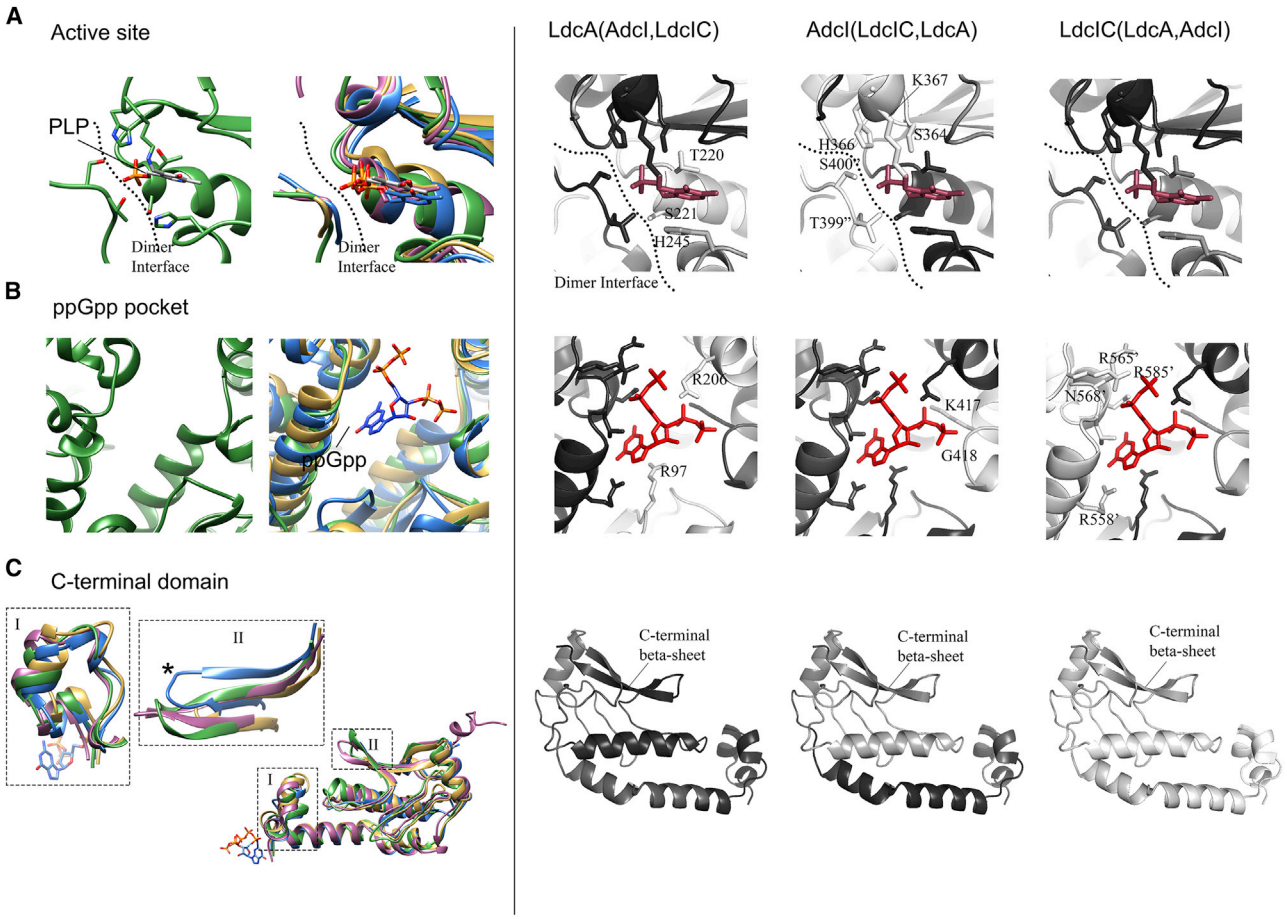

Figure 5. Close-up Views in LdcA, LdcI, AdcI, and OdcI

Left-hand side: comparison of (A) the active sites, (B) the ppGpp pockets, and (C) the C-terminal domains between the four structures, colored as in Figure 4. Right-hand side: LdcI crystal structure, shown here because it has the highest resolution, colored according to CumRelMLT values for the three possible topologies. Identity and number of the residues situated in the region supporting the topology in question are shown in each corresponding panel and in Table S5. (C) Zoom focusing on two regions described in the text: I, helices at the onset of the CTD, involved in ppGpp binding in LdcI; II, extreme C-terminal two-stranded β sheet of the protein.

suggests that LdcA may have kept ancestral features shared with OdcIC in comparison with LdcIC and AdcI that developed a tighter wing interlocking system.

The Active Site of All Lysine Decarboxylases Is Similar

The PLP-binding domain of LdcA consists of a seven-stranded mixed β sheet and flanking helices that form the cofactor binding site in a canonical type I PLP enzyme fold (Figures 2A and 5A). Overall, this domain is very similar in LdcA, LdcI, and AdcI (RMSD between them being ~1.5 Å, Table S2). A PLP moiety was modeled at the PLP-binding site of LdcA. Interestingly, in the cryo-EM map of LdcA, no density for the side chain of the strictly conserved active site lysine (K393 in LdcA, corresponding to K367 in LdcI), whose NZ atom forms a covalent bond with the C4′ atom of PLP, is visible. We believe that this is due to the instability of the lysine-PLP linkage previously described as sensitive to radiation (Dubnovitsky et al., 2005). Thus, the side chain of the active site lysine was modeled based on available structural knowledge on LdcI and AdcI, and the similarity of the PLP site as observed here.

As described above, the sliding window approach showed that the N-terminal half of the PLP-binding domain grouped together AdcI and LdcIC, to the exclusion of LdcA, whereas the C-terminal half of this domain grouped together LdcA and LdcIC, to the exclusion of AdcI (Figure 3). On the one side, half of the six active site residues involved in direct interactions with the PLP moiety in the high-resolution crystal structure of LdcI (T220, S221, and H245) and their equivalents in LdcA are situated in the N-terminal half of the PLP-binding domain, i.e., in the region supporting the LdcA(AdcI, LdcIC) topology. On the other side, the second half of the residues interacting with the PLP moiety (D330, A332, and W333 in LdcI), the key lysine forming the Schiff-base linkage with PLP (K367), and all residues making only hydrogen bonds with the phosphate group of PLP (S364, H366, T399, and S400 in LdcI), are located in the C-terminal half of this domain, i.e., in a region supporting the AdcI(LdcIC, LdcA) topology. Thus, 8 of 11 active site residues support the grouping of the lysine decarboxylases together. This observation suggests that lysine-binding capacity shared by both LdcIC and LdcA is either vertically inherited from a common ancestor or

secondary acquired following a recombination event. A summary of the LdcI residues involved in PLP binding and corresponding LdcA residues is provided in Figure 5A and Table S3.

P. aeruginosa LdcA Is Not Inhibited by the Alarmone of the Stringent Response, ppGpp

Tight binding of ppGpp to *E. coli* LdcI and LdcC (Kanjee et al., 2011b) was first revealed by a serendipitous discovery of this stringent response alarmone inside the LdcI crystal in the process of structure refinement. This ppGpp co-purified and co-crystallized with LdcI, which later led to a demonstration of the ppGpp capacity to strongly inhibit the LdcI activity *in vitro* and *in vivo*, and to stabilize the LdcI decamer at all pH values (Kanjee et al., 2011a). No additional density for ppGpp was, however, detected in the AdcI crystals, and the absence of inhibition of AdcI by ppGpp was documented (Andréll et al., 2009; Kanjee et al., 2011b). The potential ppGpp-binding pocket in our 3.7-Å resolution cryo-EM map of *P. aeruginosa* LdcA is clearly empty, although the resolution should be sufficient for an eventual visualization of this molecule. Therefore, we investigated the kinetics of lysine decarboxylation by LdcA in the absence and presence of ppGpp by isothermal titration calorimetry. We observed no significant difference in the enzymatic activity of LdcA, whereas the inhibitory effect of ppGpp on the LdcI activity (Kanjee et al., 2011a) could be clearly reproduced (Figure S4). In this respect, LdcA seems therefore to be more similar to AdcI than to LdcI and LdcC.

Remarkably, structural superposition of LdcI, LdcA, and AdcI indicated variations in the ppGpp-binding pocket at the levels of both sequence and structure. Significant differences between LdcA and LdcI that may explain the absence of ppGpp binding can be classified according to three effects: reduction of the volume of the ppGpp cavity, loss of direct interactions, and appearance of repulsive interactions (Figure 5B; Table S4). The sliding window approach shows that the ppGpp-binding domain does not support a particular topology because of a lack of signal (Figure 3). Specifically, only two of eight residues in the ppGpp-binding pocket (Figure 5B; Table S4), namely K417 and G418 in LdcI (E447 and G448 in LdcA), are situated in a region that supports grouping of LdcA with LdcIC, whereby K417 is not crucial for ppGpp binding by LdcIC because it was shown to interact with the 3′-phosphate group of ppGpp only in one of the two ppGpp conformations observed in the LdcI crystal structure (Kanjee et al., 2011a). Thus, comparison between the structure and the phylogenetic signal explains the absence of LdcA interaction with ppGpp contrary to LdcI and LdcC.

It should be noted at this point that the definition of both the N-terminal and the C-terminal boundaries of the AAT-like small domain that we adopted from the literature on LAOdcs is ambiguous. Based on the structures, the last helix of the PLP-binding domain (α20 in LdcI) may be better defined as a transition element between this domain and the AAT-like small domain. Indeed, although residues immediately upstream of this helix still contribute to interaction with PLP, residues at the C-terminal end of the same helix are directly interacting with ppGpp in the LdcI crystal structure (Figure 2; Table S4). A similar ambiguity holds for the boundary between the AAT-like small domain and the CTD which starts with four helices (α24, α25, α26, and α27 in LdcI): the first and the last helices interact with ppGpp while the middle ones participate in the fold of the CTD (Figure 2; Table S4).

The Molecular Determinant of the Interaction with RavA Is Unique to LdcI

The CTDs of all currently determined LAOdc structures are largely similar (Table S2) with the exception of two interesting regions highlighted in Figure 5C. The first region is the group of short helices at the onset of the CTD described above, and in particular residues Arg565 and Asn568, which form hydrogen bonds with the terminal phosphate groups of ppGpp in the LdcI crystal structure, but are replaced by non-interacting Pro602 and Asp605 in LdcA (Figure 5; Table S4). The second compelling region is the extreme C-terminal two stranded β sheet of the protein (Figure 5). This structural element has been previously identified as the major molecular determinant for the interaction of *E. coli* LdcI, but not LdcC, with the MoxR AAA+ ATPase RavA (Kanjee et al., 2011b; Malet et al., 2014). In our earlier work, we swapped the C-terminal β sheets between *E. coli* LdcI and LdcC, demonstrating that the presence of this structural element is necessary and sufficient for RavA binding, and identified several enterobacterial LdcI-specific residues essential for interaction with RavA (Kandiah et al., 2016). LdcI-RavA interaction results in an assembly of two LdcI decamers and five RavA hexamers into a unique 3.5-MDa cage-like complex important in particular for counteracting the *E. coli* acid stress response under starvation conditions (El Bakkouri et al., 2010; Malet et al., 2014). Our current study reveals that the loop between the two β strands is the shortest in AdcI and the longest in LdcA and OdcI. On the whole, the C-terminal β sheet nicely superimposes among OdcI, AdcI, and LdcA, but adopts a different conformation in LdcI, suggesting that the capacity to bind RavA is a distinctive feature that evolved specifically in the LdcIC subfamily.

Identification of the *ravAviaA* Operon in the Accessory Genome of *P. aeruginosa*

In *Enterobacteriaceae*, *ravA* is organized in an operon with the poorly characterized *viaA* coding for a VWA domain-containing protein termed ViaA, with VWA standing for von Willebrand factor type A domain, typically involved in protein-protein interactions (Whittaker and Hynes, 2002). Although the structural analysis presented above did not point to a possible LdcA interaction with a RavA homolog in *P. aeruginosa*, we searched for a *ravA* gene and/or a *ravAviaA* operon in the bacterium. The *P. aeruginosa* genome, whose size within the species ranges from 5.5 to 7 Mbp, is known to be composed of a conserved core genome of at ~665 genes shared among all strains (Freschi et al., 2018), and an accessory genome comprising plasmids and variable sequences inserted at various loci scattered around the genomic sequence. Genes belonging to the accessory genome, largely acquired by HGT, are mostly transposons, prophages, and genomic islands, such as integrative and conjugative elements (ICEs), which can confer advantageous phenotypes under certain conditions and is a great source of genome diversity (Hilker et al., 2015; Klockgether et al., 2011; Kung et al., 2010; Ozer et al., 2014; Tummler, 2006).

While *ldcA* is part of the core genome of *P. aeruginosa* (Carriel et al., 2018), we found that *ravAviaA* is absent in most isolates such as PAO1, PA14, and PA7, the representatives of the three

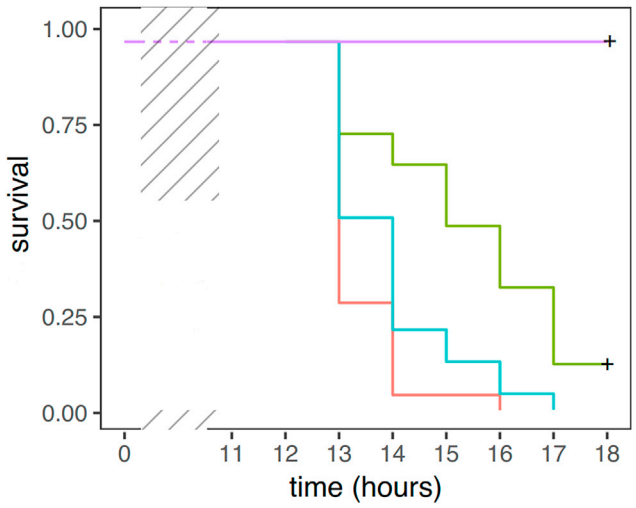

Figure 6. *ldcA* Inactivation Impacts *P. aeruginosa* Virulence in a Whole Organism

Survival of *Galleria mellonella* larvae after infection with different *P. aeruginosa* strains. Three independent experiments with a total of 25 larvae were used for each strain and combined in this plot. PBS was injected as a mock. Horizontal lines represent the survival at the indicated time point (PAO1 in pink, Δ*ldcA* in green, *ldcA::ldcA* in light blue, PSB buffer control in purple). PAO1 and Δ*ldcA::ldcA* are more virulent than Δ*ldcA*. Pairwise difference p values are PAO1 versus Δ*ldcA*: 2.6×10^{-5}; PAO1 versus Δ*ldcA::ldcA* 0.0820, and Δ*ldcA* versus Δ*ldcA::ldcA* 0.0023.

major groups of *P. aeruginosa* strains defined from phylogenetic analysis of core genome sequences (Freschi et al., 2015). Yet, 85 of a total of 4,129 *P. aeruginosa* strains available at the time of this analysis (May 2019) in the NCBI database (i.e., ~2%) were found to contain a homolog of the *ravAviaA* operon, *ravA* being systematically associated to *viaA* (Table S5). All detected genes encode proteins sharing 99% identity. The *ravAviaA* operon is situated in a genomic island previously identified in the keratitis isolate 39016 (Stewart et al., 2011), whose genomic sequence is available on the www.pseudomonas.com website (Winsor et al., 2016). This genomic island is located in the Region of Genome Plasticity RGP2, integrated at a $tRNA^{Arg}$ locus that is a hotspot for the insertion of accessory genomic elements (Kung et al., 2010). Its low guanosine/cytosine (GC) content (55.2% compared with the 65%–67% of the *P. aeruginosa* core genome) suggests its possible acquisition by an HGT event. The presence of the operon in the accessory genome indicates that, if *P. aeruginosa* LdcA does interact with RavA, this interaction would be relevant only in a very restricted number of strains. To probe formation of a putative LdcA-RavA complex, we cloned the *ravA* gene from the *P. aeruginosa* 39016 strain, produced the recombinant protein, and indeed could not detect its interaction with *P. aeruginosa* LdcA (see the STAR Methods).

Therefore, to get initial insight into the roles of the *P. aeruginosa ravA* and *viaA*, we meticulously analyzed the genetic environment of the *ravAviaA* operon in the above-mentioned 85 strains, which were isolated from a wide variety of geographical locations and environmental settings with no obvious link to any specific clinical conditions (Table S5). We found that the *ravAviaA*-harboring genomic islands appear in two main different genetic arrangements that share some of the characteristics of ICEs, such as a site-specific attachment and genes encoding phage-like integrases, but lack genes required for transmission and conjugation, e.g., for GI-type 4 pili synthesis as in transmissible ICEs (Figure S5). Strikingly, the genomic islands containing the *ravAviaA* operon always enclose elements recently identified in genomic islands that have been defined as "defense islands." These defense islands have been described to cluster genes participating in microbial defense mechanisms against phages and foreign plasmids (Doron et al., 2018). Specifically, HmmScan analysis of the most common *ravAviaA*-containing genomic island showed that 10 of 29 open reading frames encode type I restriction modification (R-M) systems, CRISPR-Cas2 and the 4-protein system JetABCD called "Wadjet" (Figure S5; Table S6). Furthermore, the second genetic arrangement of the *ravAviaA*-containing genomic island, currently found in draft genomes only, also exhibits type I R-M and Wadjet systems and encloses an additional group of genes linked to heavy-metal resistance (Figure S5; Table S6). The Wadjet system is a newly discovered broadly spread system shown to be essential for anti-plasmid defense and proposed to have been adapted from a condensin ancestor involved in bacterial chromosome maintenance to identify and fight foreign plasmids (Doron et al., 2018). The presence of *ravAviaA* in such defense islands prompts us to suggest a putative role of these proteins in innate immunity as actors of the bacterial protection against foreign plasmids and/or predatory phages.

ldcA Inactivation Impacts Full Virulence of *P. aeruginosa* in *Galleria* Host

Altogether, (1) the structural comparison of *P. aeruginosa* LdcA with *E. coli* LdcI and AdcI, and with *L. saerimneri 30a* OdcI, (2) the absence of ppGpp binding to LdcA, and (3) the divergent function of *ravAviaA* in *P. aeruginosa*, clearly show that LdcA is different from the widely studied enterobacterial LdcI. Building further on our previous work (Carriel et al., 2018), we sought to examine whether the inactivation of *ldcA* (i.e., polyamine limitation) affects *P. aeruginosa* virulence (Figure 6). To this end, we used a well-established model to study microbial infections—*Galleria mellonella* (greater wax moth) larvae—as a virulence model (Tsai et al., 2016). *G. mellonella* lacks an adaptive immune response but possesses a complex innate immune system which makes it a valuable alternative to vertebrate models. *G. mellonella* larvae were infected with the wild-type PAO1 strain, a strain with deleted *ldcA* gene (PAO1Δ*ldcA*) and the complemented mutant with a copy of the *ldcA* gene integrated in the chromosome (PAO1Δ*ldcA::ldcA*) (Carriel et al., 2018). The relative survival of the three strains was monitored over time at 37°C (Figure 6). The rate of larvae killing by the Δ*ldcA* strain was significantly slower compared with PAO1 ($p = 2.6 \times 10^{-5}$) and Δ*ldcA::ldcA* ($p = 0.0023$), whereas PAO1 and Δ*ldcA::ldcA* had a similar killing kinetics ($p = 0.082$). This demonstrates the importance of the LdcA involvement in polyamine homeostasis for the *P. aeruginosa* infection of the *Galleria* host.

DISCUSSION

Inducible AAT-fold LAOdcs have been studied since the early 1940s (Gale and Epps, 1942; Taylor and Gale, 1945) because of the link between pathogenicity of enterobacteria for their

human host and their ability to overcome the aggressive pH environments of the stomach, digestive and urinary tracts. In particular, the broad acid pH range of activity of LdcI and its capacity to promote survival and growth of *Salmonella enterica* serovar Typhimurium, *Vibrio cholerae*, and *Vibrio vulnificus* under acidic conditions are extensively documented (Kim et al., 2006; Merrell and Camilli, 1999; Viala et al., 2011). AdcI offers protection against extreme acid stress down to a pH of around 2 (Castanie-Cornet et al., 1999; Kanjee and Houry, 2013; Lin et al., 1996) and is also described to enhance survival of cells exposed to short-chain fatty acids commonly formed during fermentative growth (Guilfoyle and Hirshfield, 1996; Lin et al., 1996). OdcI, acquired by HGT from enterobacteria (Carriel et al., 2018; Romano et al., 2013), is linked to acid stress survival of lactobacilli; these lactic acid bacteria can have either beneficial probiotic activity or can on the contrary be harmful via toxic effects of their biogenic amines upon food ingestion (Ladero et al., 2010).

Recently, biosynthetic decarboxylases have attracted more attention because of the growing awareness of diverse and important roles of polyamines produced by these enzymes. For example, enhanced colonization of the bladder by uropathogenic *E. coli* (UPEC) is attributed to Cad, and the link to LdcC is clearly established (Bower et al., 2009). In addition, the level of Cad production by UPEC can be directly linked to their resistance to fluoroquinolones, antibiotics routinely used as a first-line treatment of urinary tract infections (Akhova and Tkachenko, 2009; Kikuchi et al., 1997). Furthermore, Cad induces closure of the outer membrane porins OmpC and OmpF, thereby contributing to bacterial protection from acid stress, but also from certain antibiotics, and to reduction of membrane permeability in *E. coli* (Dela Vega and Delcour, 1996; Zhao and Houry, 2010). Moreover, an AAT-fold Ldc from *Eikenella corrodens*, a commensal bacterium of human dental biofilm, was described as a virulence factor that affects the dental epithelial barrier to bacterial proinflammatory products by locally depleting lysine, an essential nutrient for mammalian cells (Lohinai et al., 2012, 2015). Interestingly, LdcI has been shown to negatively regulate virulence in several enteric pathogens including enterohemorrhagic *E. coli* (Torres, 2009; Vazquez-Juarez et al., 2008).

P. aeruginosa is often associated with severe and life-threatening infections, especially in immunocompromised individuals, such as burn victims, and in cystic fibrosis patients where it forms a resilient biofilm leading in particular to pulmonary tissue destruction. We recently reported that LdcA from *P. aeruginosa* PAO1 exerts its function through Cad biosynthesis and concomitant regulation of intracellular levels of Put and Spd (Carriel et al., 2018). Specifically, disruption of the *ldcA* gene and the resulting absence of Cad appear to modulate the general polyamine metabolism of *P. aeruginosa* (Carriel et al., 2018), thereby generating strong pleiotropic effects. From this perspective, the impaired virulence of the *ldcA* mutant in the *Galleria* model presented here can be interpreted in terms of the importance of Cad and more generally of polyamines in *P. aeruginosa* growth and/or expression of virulence genes (Turner et al., 2014). Altogether, considering that Cad synthesized by LdcA enhances *P. aeruginosa* growth fitness (Carriel et al., 2018) and infection process, LdcA can be regarded as an important modulator of polyamine homeostasis and an additional player in the physiology of this opportunistic pathogen. We anticipate that these studies and the structure of the LdcA determined in the current manuscript serve as the basis to establish LdcA as a potential target for therapeutic interventions.

The presented phylogenetic analysis uses an unconventional sliding window approach and offers insights into the evolutionary history of LAdcs. In particular, it reveals conflicting phylogenetic signals contained in the sequences, with the N-terminal region supporting a close relationship between AdcI and LdcIC, to the exclusion of LdcA, while the middle region favors a proximity between LdcIC and LdcA, and the C-terminal region groups LdcA with AdcI. This observation, along with a weak phylogenetic signal supporting the monophyly of AdcI and, to a lesser extent, of LdcA, suggests possible recombination events between members of these subfamilies, and provides an explanation why LdcA, LdcIC, and Adc two by two share common features. Worthy of note, the phylogenetic signal shifts occurred within structural/functional domains, contradicting the classical picture where structural domains are considered as coherent blocks from an evolutionary point of view. More generally, we believe that the sliding window approach as applied here could be of a great assistance in functional dissection and precise comparison of homologous protein structures.

As shown by us and by others (Burrell et al., 2010; Carriel et al., 2018; Kanjee et al., 2011b), the proteobacterial LAOdcs evolved from shorter-wing domain-less LAOdcs characteristic of *Actinobacteria*, *Cyanobacteria*, and *Firmicutes* AAT-fold decarboxylases, by fusion with a CheY-like response regulator receiver domain that occurred in *Proteobacteria* and probably during the diversification of *Beta-* and *Gammaproteobacteria*. This fusion seems to be a pre-requisite for formation of higher-order ring assemblies by lateral and in certain cases pH-dependent interactions between wing domains. Nonetheless, some LAOdcs, for example *E. coli* OdcC and OdcI, are dimeric despite the presence of the wing domains, although the OdcI from *L. saerimneri 30a* is a dodecamer (Kanjee et al., 2011b; Momany et al., 1995). Here we show that, although wing-wing interactions between dimeric building blocks in *L. saerimneri 30a* OdcI and in *P. aeruginosa* LdcA are similarly weakened by the absence of the helical wing interlocking system (Figure 4), the latter is still a stable decamer. High-order oligomerization is essential for the enzymatic activity of *L. saerimneri 30a* OdcI and *E. coli* AdcI, but not of *E. coli* LdcI and LdcC (Kanjee et al., 2011b), suggesting that the wing-domain function may be more elaborate than the stabilization of the double-toroidal architecture.

The absence of ppGpp-dependent inhibition of *P. aeruginosa* LdcA may seem surprising considering that both *E. coli* LdcI and LdcC are strongly inhibited by this stringent response alarmone (Kanjee et al., 2011b). Yet, our analysis indicates that this property was acquired specifically by the LdcIC ancestor. Considering Cad as an important platform chemical for the synthesis of industrial polymers such as nylon as well as environmentally friendly bio-based polyamides, and given the currently exclusive usage of LdcIC enzymes for industrial Cad production (Ma et al., 2017), exploiting information contained in the 3D structure of LdcA may prove useful for optimization of bacterial Cad-producing strains toward increased profitability of bio-based polyamides.

Finally, our structural and evolutionary comparison of the CTDs of LdcI, LdcA, AdcI, and OdcI, and in particular of the

C-terminal β sheet responsible for the specific nanomolar affinity interaction of enterobacterial LdcI with the MoxR AAA+ ATPase RavA, immediately implied that *P. aeruginosa* LdcA should not be able to form a complex with RavA. The fact that we found the *ravAviaA* operon not to belong to the core genome of *P. aeruginosa* corroborated this hypothesis. In this light, our discovery of this operon in the RGP2 of 85 *P. aeruginosa* strains, its low GC content pointing to a possible acquisition through horizontal transfer, and extremely high sequence conservation of RavA and ViaA in all *ravAviaA*-containing *P. aeruginosa* strains, were puzzling, and suggested an eventually different, LdcA-independent, function of RavA and ViaA in these strains. Interestingly, several reports on *E. coli* RavA and ViaA mention their functional link with bacterial respiration and iron-sulfur cluster biogenesis (Babu et al., 2014; Wong and Houry, 2012; Wong et al., 2017). In particular, the *E. coli* RavA-ViaA system was proposed to act as a chaperone of the fumarate reductase FrdA protein (Wong et al., 2017). Our analysis of the genetic environment of the *ravAviaA* operon in *P. aeruginosa* points to yet another exciting role of these genes. Specifically, this operon clearly resides in between defense systems such as type I R-M and Wadjet involved in phage and plasmid resistance, respectively, suggestive of anti-phage and/or anti-plasmid defensive functions of RavA and ViaA. Indeed, many recent studies focused on individual genes of unknown function inside known genomic defense islands revealed that these genes themselves also contribute to the defensive arsenal and enabled discoveries of novel systems protecting bacteria against phages and foreign plasmids (Doron et al., 2018). An observation that a ViaA homolog p892 from the crenarchaeal *Acidianus* two-tailed virus ATV could nonspecifically bind DNA *in vitro* (Scheele et al., 2011) may in this respect be of potential interest. A putative defensive role of *ravAviaA* in *P. aeruginosa* and eventually in other microbial genomes opens up an alternative direction for further research. In addition, *ldcA* being present in the core genome while *ravAviaA* is contained in the accessory genome of *P. aeruginosa* implies that coevolution of the two systems may be specific to enterobacteria and deserves future investigation.

STAR★METHODS

Detailed methods are provided in the online version of this paper and include the following:

- KEY RESOURCES TABLE
- LEAD CONTACT AND MATERIALS AVAILABILITY
- EXPERIMENTAL MODEL AND SUBJECT DETAILS
- METHOD DETAILS
  - Protein Expression and Purification
  - Cryo-EM Data Collection and 3D Reconstruction
  - Model Building, Refinement and Validation
  - Isothermal Titration Calorimetry
  - Analysis of the *P. aeruginosa ravAviaA* Operon
  - Phylogeny: Dataset Assembly
  - Phylogeny: Phylogenetic Inference
  - Phylogeny: Sliding Window Approach
  - *Galleria mellonella* Treatment Assays
- QUANTIFICATION AND STATISTICAL ANALYSIS
- DATA AND CODE AVAILABILITY

SUPPLEMENTAL INFORMATION

Supplemental Information can be found online at https://doi.org/10.1016/j.str.2019.10.003.

ACKNOWLEDGMENTS

We thank Guy Schoehn for establishing and managing the cryoelectron microscopy platform and for providing training and support, and Aymeric Peuch for help with the usage of the EM computing cluster. This work has received funding from the European Union's Horizon 2020 research and innovation program under grant agreement no. 647784, GRAL (ANR-10-LABX-49-01), and the ANR-16-CE02-0005. We used the platforms of the Grenoble Instruct-ERIC Center (ISBG: UMS 3518 CNRS-CEA-UGA-EMBL) with support from FRISBI (ANR-10-INSB-05-02) and GRAL (ANR-10-LABX-49-01) within the Grenoble Partnership for Structural Biology (PSB). The electron microscope facility is supported by the Rhône-Alpes Region, the Fondation pour la Recherche Médicale (FRM), the fonds FEDER, the Centre National de la Recherche Scientifique (CNRS), the Commissariat à l'Energie Atomique et aux Energies Alternatives (CEA), the Université Grenoble Alpes (UGA), EMBL, and the GIS-Infrastructures en Biologie Santé et Agronomie (IBISA). D.C. was supported by a PhD grant from LABEX GRAL, P.S.G. was supported by a PhD grant from ARC1 Santé Rhône-Alpes Auvergne, and J.F. was supported by a long-term EMBO fellowship (ALTF441-2017).

AUTHOR CONTRIBUTIONS

All authors performed experiments and analyzed data. I.G. designed the overall study and supervised the project with the help of S.E. for the functional part, and C.B.-A. for the phylogeny part. I.G. wrote the paper with contributions from all authors.

DECLARATION OF INTERESTS

The authors declare no competing interests.

Received: June 4, 2019
Revised: September 9, 2019
Accepted: October 1, 2019
Published: October 22, 2019

REFERENCES

Adams, P.D., Afonine, P.V., Bunkóczi, G., Chen, V.B., Davis, I.W., Echols, N., Headd, J.J., Hung, L.-W., Kapral, G.J., Grosse-Kunstleve, R.W., et al. (2010). PHENIX: a comprehensive Python-based system for macromolecular structure solution. Acta Crystallogr. D. Biol. Crystallogr. *66*, 213–221.

Akhova, A.V., and Tkachenko, A.G. (2009). Lysine decarboxylase activity as a factor of fluoroquinolone resistance in *Escherichia coli*. Microbiology *78*, 575–579.

Altschul, S.F., Madden, T.L., Schäffer, A.A., Zhang, J., Zhang, Z., Miller, W., and Lipman, D.J. (1997). Gapped BLAST and PSI-BLAST: a new generation of protein database search programs. Nucleic Acids Res. *25*, 3389–3402.

Andréll, J., Hicks, M.G., Palmer, T., Carpenter, E.P., Iwata, S., and Maher, M.J. (2009). Crystal structure of the acid-induced arginine decarboxylase from *Escherichia coli*: reversible decamer assembly controls enzyme activity. Biochemistry *48*, 3915–3927.

Babu, M., Arnold, R., Bundalovic-Torma, C., Gagarinova, A., Wong, K.S., Kumar, A., Stewart, G., Samanfar, B., Aoki, H., Wagih, O., et al. (2014). Quantitative genome-wide genetic interaction screens reveal global epistatic relationships of protein complexes in *Escherichia coli*. PLoS Genet. *10*, e1004120.

El Bakkouri, M., Gutsche, I., Kanjee, U., Zhao, B., Yu, M., Goret, G., Schoehn, G., Burmeister, W.P., and Houry, W.A. (2010). Structure of RavA MoxR AAA+ protein reveals the design principles of a molecular cage modulating the inducible lysine decarboxylase activity. Proc. Natl. Acad. Sci. U S A *107*, 22499–22504.

Benjamini, Y., and Hochberg, Y. (1995). Controlling the false discovery rate—a practical and powerful approach to multiple testing. J. R. Stat. Soc. Ser. B Methodol. *57*, 289–300.

Bland, J.M., and Altman, D.G. (1986). Statistical methods for assessing agreement between two methods of clinical measurement. Lancet (London, England) *1*, 307–310.

Bower, J.M., Gordon-Raagas, H.B., and Mulvey, M.A. (2009). Conditioning of uropathogenic *Escherichia coli* for enhanced colonization of host. Infect. Immun. *77*, 2104–2112.

Burrell, M., Hanfrey, C.C., Murray, E.J., Stanley-Wall, N.R., and Michael, A.J. (2010). Evolution and multiplicity of arginine decarboxylases in polyamine biosynthesis and essential role in *Bacillus subtilis* biofilm formation. J. Biol. Chem. *285*, 39224–39238.

Carriel, D., Simon Garcia, P., Castelli, F., Lamourette, P., Fenaille, F., Brochier-Armanet, C., Elsen, S., and Gutsche, I. (2018). A novel subfamily of bacterial AAT-fold basic amino acid decarboxylases and functional characterization of its first representative: *Pseudomonas aeruginosa* LdcA. Genome Biol. Evol. *10*, 3058–3075.

Castanie-Cornet, M.-P., Penfound, T.A., Smith, D., Elliott, J.F., and Foster, J.W. (1999). Control of acid resistance in *Escherichia coli*. J. Bacteriol. *181*, 3525–3535.

Chen, V.B., Arendall, W.B., Headd, J.J., Keedy, D.A., Immormino, R.M., Kapral, G.J., Murray, L.W., Richardson, J.S., and Richardson, D.C. (2010). MolProbity: all-atom structure validation for macromolecular crystallography. Acta Crystallogr. D. Biol. Crystallogr. *66*, 12–21.

Chou, H.T., Hegazy, M., and Lu, C.D. (2010). L-Lysine catabolism is controlled by L-arginine and ArgR in *Pseudomonas aeruginosa* PAO1. J. Bacteriol. *192*, 5874–5880.

Criscuolo, A., and Gribaldo, S. (2010). BMGE (Block Mapping and Gathering with Entropy): a new software for selection of phylogenetic informative regions from multiple sequence alignments. BMC Evol. Biol. *10*, 210.

Dela Vega, A.L., and Delcour, A.H. (1996). Polyamines decrease *Escherichia coli* outer membrane permeability. J. Bacteriol. *178*, 3715–3721.

Desbois, A.P., and Coote, P.J. (2011). Wax moth larva (Galleria mellonella): an in vivo model for assessing the efficacy of antistaphylococcal agents. J. Antimicrob. Chemother. *66*, 1785–1790.

Doron, S., Melamed, S., Ofir, G., Leavitt, A., Lopatina, A., Keren, M., Amitai, G., and Sorek, R. (2018). Systematic discovery of antiphage defense systems in the microbial pangenome. Science *359*, https://doi.org/10.1126/science.aar4120.

Dubnovitsky, A.P., Ravelli, R.B.G., Popov, A.N., and Papageorgiou, A.C. (2005). Strain relief at the active site of phosphoserine aminotransferase induced by radiation damage. Protein Sci. *14*, 1498–1507.

Dubochet, J., Adrian, M., Chang, J.J., Homo, J.C., Lepault, J., McDowall, A.W., and Schultz, P. (1988). Cryo-electron microscopy of vitrified specimens. Q. Rev. Biophys. *21*, 129–228.

Emsley, P., and Cowtan, K. (2004). Coot: model-building tools for molecular graphics. Acta Crystallogr. D. Biol. Crystallogr. *60*, 2126–2132.

Freschi, L., Jeukens, J., Kukavica-Ibrulj, I., Boyle, B., Dupont, M.-J., Laroche, J., Larose, S., Maaroufi, H., Fothergill, J.L., Moore, M., et al. (2015). Clinical utilization of genomics data produced by the international *Pseudomonas aeruginosa* consortium. Front. Microbiol. *6*, 1036.

Freschi, L., Vincent, A.T., Jeukens, J., Emond-Rheault, J.-G., Kukavica-Ibrulj, I., Dupont, M.-J., Charette, S.J., Boyle, B., and Levesque, R.C. (2018). The *Pseudomonas aeruginosa* pan-genome provides new insights on its population structure, horizontal gene transfer and pathogenicity. Genome Biol. Evol. *11*, 109–120.

Gale, E.F., and Epps, H.M. (1942). The effect of the pH of the medium during growth on the enzymic activities of bacteria (*Escherichia coli* and *Micrococcus lysodeikticus*) and the biological significance of the changes produced. Biochem. J. *36*, 600–618.

Gouy, M., Guindon, S., and Gascuel, O. (2010). SeaView version 4: a multiplatform graphical user interface for sequence alignment and phylogenetic tree building. Mol. Biol. Evol. *27*, 221–224.

Gribaldo, S., and Brochier, C. (2009). Phylogeny of prokaryotes: does it exist and why should we care? Res. Microbiol. *160*, 513–521.

Guilfoyle, D.E., and Hirshfield, I.N. (1996). The survival benefit of short-chain organic acids and the inducible arginine and lysine decarboxylase genes for *Escherichia coli*. Lett. Appl. Microbiol. *22*, 393–396.

Guindon, S., Dufayard, J.-F., Lefort, V., Anisimova, M., Hordijk, W., and Gascuel, O. (2010). New algorithms and methods to estimate maximum-likelihood phylogenies: assessing the performance of PhyML 3.0. Syst. Biol. *59*, 307–321.

Hilker, R., Munder, A., Klockgether, J., Losada, P.M., Chouvarine, P., Cramer, N., Davenport, C.F., Dethlefsen, S., Fischer, S., Peng, H., et al. (2015). Interclonal gradient of virulence in the *Pseudomonas aeruginosa* pangenome from disease and environment. Environ. Microbiol. *17*, 29–46.

Huerta-Cepas, J., Serra, F., and Bork, P. (2016). Ete 3: reconstruction, analysis, and visualization of phylogenomic data. Mol. Biol. Evol. *33*, 1635–1638.

Huson, D.H., and Bryant, D. (2006). Application of phylogenetic networks in evolutionary studies. Mol. Biol. Evol. *23*, 254–267.

Kandiah, E., Carriel, D., Perard, J., Malet, H., Bacia, M., Liu, K., Chan, S.W.S.S., Houry, W.A., Ollagnier de Choudens, S., Elsen, S., et al. (2016). Structural insights into the *Escherichia coli* lysine decarboxylases and molecular determinants of interaction with the AAA+ ATPase RavA. Sci. Rep. *6*, 24601.

Kanjee, U., and Houry, W.A. (2013). Mechanisms of acid resistance in *Escherichia coli*. Annu. Rev. Microbiol. *67*, 65–81.

Kanjee, U., Gutsche, I., Alexopoulos, E., Zhao, B., El Bakkouri, M., Thibault, G., Liu, K., Ramachandran, S., Snider, J., Pai, E.F., et al. (2011a). Linkage between the bacterial acid stress and stringent responses: the structure of the inducible lysine decarboxylase. EMBO J. *30*, 931–944.

Kanjee, U., Gutsche, I., Ramachandran, S., and Houry, W.A. (2011b). The enzymatic activities of the *Escherichia coli* basic aliphatic amino acid decarboxylases exhibit a pH zone of inhibition. Biochemistry *50*, 9388–9398.

Katoh, K., and Standley, D.M. (2013). MAFFT multiple sequence alignment software version 7: improvements in performance and usability. Mol. Biol. Evol. *30*, 772–780.

Kelley, L.A., Mezulis, S., Yates, C.M., Wass, M.N., and Sternberg, M.J.E. (2015). The Phyre2 web portal for protein modeling, prediction and analysis. Nat. Protoc. *10*, 845–858.

Kikuchi, Y., Kojima, H., Tanaka, T., Takatsuka, Y., and Kamio, Y. (1997). Characterization of a second lysine decarboxylase isolated from *Escherichia coli*. J. Bacteriol. *179*, 4486–4492.

Kim, J.-S., Choi, S.H., and Lee, J.K. (2006). Lysine decarboxylase expression by *Vibrio vulnificus* is induced by SoxR in response to superoxide stress. J. Bacteriol. *188*, 8586–8592.

Klockgether, J., Cramer, N., Wiehlmann, L., Davenport, C.F., and Tümmler, B. (2011). *Pseudomonas aeruginosa* genomic structure and diversity. Front. Microbiol. *2*, 150.

Kucukelbir, A., Sigworth, F.J., and Tagare, H.D. (2014). Quantifying the local resolution of cryo-EM density maps. Nat. Methods *11*, 63–65.

Kung, V.L., Ozer, E.A., and Hauser, A.R. (2010). The accessory genome of *Pseudomonas aeruginosa*. Microbiol. Mol. Biol. Rev. *74*, 621–641.

Ladero, V., Calles-Enríquez, M., Fernández, M., and Alvarez, M.A. (2010). Toxicological. 470 effects of dietary biogenic amines. Curr. Nutr. Food Sci. *6*, 145–156.

Larsson, A. (2014). AliView: a fast and lightweight alignment viewer and editor for large datasets. Bioinformatics *30*, 3276–3278.

Letunic, I., and Bork, P. (2016). Interactive tree of life (iTOL) v3: an online tool for the display and annotation of phylogenetic and other trees. Nucleic Acids Res. *44*, W242–W245.

Lin, J., Smith, M.P., Chapin, K.C., Baik, H.S., Bennett, G.N., and Foster, J.W. (1996). Mechanisms of acid resistance in enterohemorrhagic *Escherichia coli*. Appl. Environ. Microbiol. *62*, 3094–3100.

Lohinai, Z., Keremi, B., Szoko, E., Tabi, T., Szabo, C., Tulassay, Z., and Levine, M. (2012). Bacterial lysine decarboxylase influences human dental biofilm

lysine content, biofilm accumulation, and subclinical gingival inflammation. J. Periodontol. *83*, 1048–1056.

Lohinai, Z., Keremi, B., Szöko, E., Tábi, T., Szabo, C., Tulassay, Z., DiCesare, J.C., Davis, C.A., Collins, L.M., and Levine, M. (2015). Biofilm lysine decarboxylase, a new therapeutic target for periodontal inflammation. J. Periodontol. *86*, 1176–1184.

Lopéz-Blanco, J.R., and Chacón, P. (2013). iMODFIT: efficient and robust flexible fitting based on vibrational analysis in internal coordinates. J. Struct. Biol. *184*, 261–270.

Lu, C.-D., Yang, Z., and Li, W. (2004). Transcriptome analysis of the ArgR regulon in *Pseudomonas aeruginosa*. J. Bacteriol. *186*, 3855–3861.

Ma, W., Chen, K., Li, Y., Hao, N., Wang, X., and Ouyang, P. (2017). Advances in cadaverine bacterial production and its applications. Engineering *3*, 308–317.

Malet, H., Liu, K., El Bakkouri, M., Chan, S.W.a.S., Effantin, G., Bacia, M., Houry, W.A., and Gutsche, I. (2014). Assembly principles of a unique cage formed by hexameric and decameric *E. coli* proteins. Elife *3*, e03653.

McClure, M.A., Smith, C., and Elton, P. (1996). Parameterization studies for the SAM and HMMER methods of hidden Markov model generation. Proc. Int. Conf. Intell. Syst. Mol. Biol. *4*, 155–164.

Merrell, D.S., and Camilli, A. (1999). The cadA gene of *Vibrio cholerae* is induced during infection and plays a role in acid tolerance. Mol. Microbiol. *34*, 836–849.

Michael, A.J. (2016a). Polyamines in eukaryotes, bacteria, and archaea. J. Biol. Chem. *291*, 14896–14903.

Michael, A.J. (2016b). Biosynthesis of polyamines and polyamine-containing molecules. Biochem. J. *473*, 2315–2329.

Momany, C., Ernst, S., Ghosh, R., Chang, N.L., and Hackert, M.L. (1995). Crystallographic structure of a PLP-dependent ornithine decarboxylase from *Lactobacillus* 30a to 3.0 Å resolution. J. Mol. Biol. *252*, 643–655.

Moradali, M.F., Ghods, S., and Rehm, B.H.A. (2017). *Pseudomonas aeruginosa* lifestyle: a paradigm for adaptation, survival, and persistence. Front. Cell. Infect. Microbiol. *7*, 39.

Nguyen, L.-T., Schmidt, H.A., von Haeseler, A., and Minh, B.Q. (2015). IQ-TREE: a fast and effective stochastic algorithm for estimating maximum-likelihood phylogenies. Mol. Biol. Evol. *32*, 268–274.

Ozer, E.A., Allen, J.P., and Hauser, A.R. (2014). Characterization of the core and accessory genomes of *Pseudomonas aeruginosa* using bioinformatic tools Spine and AGEnt. BMC Genomics *15*, 737.

Pettersen, E.F., Goddard, T.D., Huang, C.C., Couch, G.S., Greenblatt, D.M., Meng, E.C., and Ferrin, T.E. (2004). UCSF Chimera—a visualization system for exploratory research and analysis. J. Comput. Chem. *25*, 1605–1612.

Ramarao, N., Nielsen-Leroux, C., and Lereclus, D. (2012). The insect *Galleria mellonella* as a powerful infection model to investigate bacterial pathogenesis. J. Vis. Exp. e4392, https://doi.org/10.3791/4392.

Romano, A., Trip, H., Lolkema, J.S., and Lucas, P.M. (2013). Three-component lysine/ornithine decarboxylation system in *Lactobacillus saerimneri* 30a. J. Bacteriol. *195*, 1249–1254.

Scheele, U., Erdmann, S., Ungewickell, E.J., Felisberto-Rodrigues, C., Ortiz-Lombardia, M., and Garrett, R.A. (2011). Chaperone role for proteins p618 and p892 in the extracellular tail development of *Acidianus* two-tailed virus. J. Virol. *85*, 4812–4821.

Scheres, S.H.W., and Chen, S. (2012). Prevention of overfitting in cryo-EM structure determination. Nat. Methods *9*, 853–854.

Snider, J., Gutsche, I., Lin, M., Baby, S., Cox, B., Butland, G., Greenblatt, J., Emili, A., and Houry, W.A. (2006). Formation of a distinctive complex between the inducible bacterial lysine decarboxylase and a novel AAA+ ATPase. J. Biol. Chem. *281*, 1532–1546.

Stewart, R.M.K., Wiehlmann, L., Ashelford, K.E., Preston, S.J., Frimmersdorf, E., Campbell, B.J., Neal, T.J., Hall, N., Tuft, S., Kaye, S.B., et al. (2011). Genetic characterization indicates that a specific subpopulation of *Pseudomonas aeruginosa* is associated with keratitis infections. J. Clin. Microbiol. *49*, 993–1003.

Taylor, E.S., and Gale, E.F. (1945). Studies on bacterial amino-acid decarboxylases: 1. l(+)-lysine decarboxylase. Biochem. J. *39*, 52–58.

Torres, A.G. (2009). The cad locus of *Enterobacteriaceae*: more than just lysine decarboxylation. Anaerobe *15*, 1–6.

Tsai, C.J.-Y., Loh, J.M.S., and Proft, T. (2016). *Galleria mellonella* infection models for the study of bacterial diseases and for antimicrobial drug testing. Virulence *7*, 214–229.

Tummler, B. (2006). Clonal variations of *Pseudomonas aeruginosa*. In Pseudomonas, *4*, J.L. Ramos and R.C. Levesque, eds. (Springer), pp. 35–68.

Turner, K.H., Everett, J., Trivedi, U., Rumbaugh, K.P., and Whiteley, M. (2014). Requirements for *Pseudomonas aeruginosa* acute burn and chronic surgical wound infection. PLoS Genet. *10*, e1004518.

Vazquez-Juarez, R.C., Kuriakose, J.A., Rasko, D.A., Ritchie, J.M., Kendall, M.M., Slater, T.M., Sinha, M., Luxon, B.A., Popov, V.L., Waldor, M.K., et al. (2008). CadA negatively regulates *Escherichia coli* O157:H7 adherence and intestinal colonization. Infect. Immun. *76*, 5072–5081.

Viala, J.P.M., Méresse, S., Pocachard, B., Guilhon, A.A., Aussel, L., and Barras, F. (2011). Sensing and adaptation to low pH mediated by inducible amino acid decarboxylases in Salmonella. PLoS One *6*, e22397.

Whittaker, C.A., and Hynes, R.O. (2002). Distribution and evolution of von Willebrand/integrin A domains: widely dispersed domains with roles in cell adhesion and elsewhere. Mol. Biol. Cell *13*, 3369–3387.

Winsor, G.L., Griffiths, E.J., Lo, R., Dhillon, B.K., Shay, J.A., and Brinkman, F.S.L. (2016). Enhanced annotations and features for comparing thousands of *Pseudomonas* genomes in the *Pseudomonas* genome database. Nucleic Acids Res. *44*, D646–D653.

Winstanley, C., O'Brien, S., and Brockhurst, M.A. (2016). *Pseudomonas aeruginosa* evolutionary adaptation and diversification in cystic fibrosis chronic lung infections. Trends Microbiol. *24*, 327–337.

Wong, K.S., and Houry, W.A. (2012). Novel structural and functional insights into the MoxR family of AAA+ ATPases. J. Struct. Biol. *179*, 211–221.

Wong, K.S., Bhandari, V., Janga, S.C., and Houry, W.A. (2017). The RavA-ViaA chaperone-like system interacts with and modulates the activity of the fumarate reductase respiratory complex. J. Mol. Biol. *429*, 324–344.

Zhang, K. (2016). Gctf: real-time CTF determination and correction. J. Struct. Biol. *193*, 1–12.

Zhao, B., and Houry, W.A. (2010). Acid stress response in enteropathogenic gammaproteobacteria: an aptitude for survival. Biochem. Cell Biol. *88*, 301–314.

Zivanov, J., Nakane, T., Forsberg, B.O., Kimanius, D., Hagen, W.J., Lindahl, E., and Scheres, S.H. (2018). New tools for automated high-resolution cryo-EM structure determination in RELION-3. Elife *7*, e42166.

STAR★METHODS

KEY RESOURCES TABLE

REAGENT or RESOURCE	SOURCE	IDENTIFIER
Bacterial and Virus Strains		
P. aeruginosa PAO1	J. Mougous laboratory, (Carriel et al., 2018)	N/A
P. aeruginosa PAO1 *ΔldcA*	(Carriel et al., 2018)	N/A
P. aeruginosa PAO1 *ΔldcA::ldcA*	(Carriel et al., 2018)	N/A
E. coli Rosetta 2 (DE3)	Novagen, Merck	71400-3
E. coli MG1655 Δ*rel*A Δ*spo*T+pT7POL26-Kan^R	F. Barras laboratory, This study	N/A
E. coli MG1655 Δ*rel*A Δ*spo*T+pT7POL26-Gm^R	F. Barras laboratory, This study	N/A
Biological Samples		
G. mellonella larvae (greater wax moth)	TrueLarv UK Ltd. (Exeter, UK)	N/A
Chemicals, Peptides, and Recombinant Proteins		
ppGpp	Jena Bioscience	NU-884L
P. aeruginosa PAO1 LdcA	This study	N/A
P. aeruginosa 39016 RavA	This study	N/A
Deposited Data		
Cryo-EM map of LdcA	This study	EMDB: 4468
Atomic model of LdcA	This study	PDB: 6Q6I
Crystal structure of LdcI	Kanjee et al., 2011a	PDB: 3N75
Crystal structure of AdcI	Andréll et al., 2009	PDB: 2VYC
Crystal structure of OdcI	Momany et al., 1995	PDB: 1ORD
Experimental Models: Organisms/Strains		
pET15b-derived p11 containing a C-terminal TEV-cleavable 6x His-tag sequence	Novagen, This study	69661
pET-29b(+) containing a C-terminal thrombin protease cleavable 6X His-tag sequence	Novagen, This study	69872
Recombinant DNA		
P. aeruginosa PAO1 ldcA	(Carriel et al., 2018)	N/A
*P. aeruginosa 39016 rav*A	GeneScript, This study	N/A
Software and Algorithms		
Gctf	(Zhang, 2016)	https://www.mrc-lmb.cam.ac.uk/kzhang/
RELION 3.0	(Zivanov et al., 2018)	https://www3.mrc-lmb.cam.ac.uk/relion/index.php/Main_Page
ResMap	(Kucukelbir et al., 2014)	http://resmap.sourceforge.net/
UCSF Chimera	(Pettersen et al., 2004)	https://www.cgl.ucsf.edu/chimera/
Phyre2	(Kelley et al., 2015)	http://www.sbg.bio.ic.ac.uk/phyre2/html/page.cgi?id=index
IMODFIT	(Lopéz-Blanco and Chacón, 2013)	http://chaconlab.org/hybrid4EM/imodfit
Phenix	(Adams et al., 2010)	http://www.phenix-online.org/
COOT	(Emsley and Cowtan, 2004)	https://www2.mrc-lmb.cam.ac.uk/Personal/pemsley/coot/
MolProbity	(Chen et al., 2010)	http://molprobity.biochem.duke.edu/
BLASTP 2.2.6	(Altschul et al., 1997)	
GeneSpy		(http://lbbe.univ-lyon1.fr/GeneSpy/index.html)
Origin ITC data analysis software	MicroCal	https://www.malvernpanalytical.com

(*Continued on next page*)

Continued

REAGENT or RESOURCE	SOURCE	IDENTIFIER
MAFFT v7	(Katoh and Standley, 2013)	https://mafft.cbrc.jp/alignment/software/
HMMER v3.1b1 package	(McClure et al., 1996)	http://hmmer.org/
BMGE v1.1	(Criscuolo and Gribaldo, 2010)	https://ngphylogeny.fr/workflows/advanced/
PhyML 3.1	(Guindon et al., 2010)	https://ngphylogeny.fr/workflows/advanced/
IQ-TREE v1.4.1	(Nguyen et al., 2015)	http://www.iqtree.org/
aliview 1.21	(Larsson, 2014)	http://ormbunkar.se/aliview/
iTOL	(Letunic and Bork, 2016)	https://itol.embl.de/
seaview 4.6.4	(Gouy et al., 2010)	http://doua.prabi.fr/software/seaview
SplitTree 4	(Huson and Bryant, 2006)	http://ab.inf.uni-tuebingen.de/software/splitstree4/
Other		
Quantifoil R1.2/1.3 holey carbon film on copper 300 mesh grids	(Quantifoil Micro Tools GmbH, Germany)	N1-C14nCu30-01

LEAD CONTACT AND MATERIALS AVAILABILITY

Further information and requests for resources and reagents should be directed to and will be fulfilled by the Lead Contact, Irina Gutsche (irina.gutsche@ibs.fr).

EXPERIMENTAL MODEL AND SUBJECT DETAILS

E. coli Rosetta 2 (DE3) cells were grown in LB medium supplemented with kanamycin and chloramphenicol at 37°C. Kan^R or Gm^R *E. coli* MG1655-derived Δ*rel*A Δ*spo*T strains were grown at 37°C in LB medium supplemented with kanamycin or gentamicine respectively. *P. aeruginosa* PAO1, PAO1*ΔldcA and* PAO1*ΔldcA::ldcA* cells were grown overnight in LB, then diluted in fresh LB to OD600 0.1 and further grown during 2 hours at 37°C under agitation. *G. mellonella* larvae were stored in Petri dishes in the dark at room temperature until the infection.

G. mellonella larvae supplied byTruLarv™ were age and weight defined from a dedicated breeding colony which does not use antimicrobials or hormones. Upon arrival, *G. mellonella* larvae were stored in Petri dishes in the dark at 16°C for no longer than two weeks until usage. For survival assays, infected *G. mellonella* larvae were incubated at 37°C.

METHOD DETAILS

Protein Expression and Purification

The *ldcA* coding sequence was cloned in the pET-29b(+) (Novagen) vector containing a C-terminal thrombin protease cleavable 6X His-tag sequence. The protein was overproduced in Rosetta 2 (DE3) cells (Novagen) in LB medium supplemented with kanamycin and chloramphenicol at 37°C, upon overnight induction with 0.5 mM IPTG at 18°C. Cell pellets were suspended in a 25 mM Tris-HCl, 300 mM NaCl, pH 7.5 buffer supplemented with Complete EDTA free (Roche), 0.1 mM PLP and 5% glycerol and subsequently disrupted by homogenizer at 4°C. Clarified supernatant was loaded on a Ni-NTA column and eluted with 500mM imidazole. After extensive dialysis to remove the imidazole, the protein was further concentrated and purified by size-exclusion chromatography (SEC) on a Superose-6 column. The protein was stored in 25 mM Tris-HCl, 300 mM NaCl, pH 7.5 buffer with 0.1 mM PLP, 1 mM DTT and 5% glycerol.

The *ravA* coding sequence from *P. aeruginosa* 39016 was cloned in the p11 plasmid, a modified pET15b (Novagen) containing a C-terminal TEV-cleavable 6x His-tag sequence. The RavA protein was expressed and purified as described for *E. coli* RavA (Snider et al., 2006). Three independent methods, including SEC-MALLS, negative stain EM and surface plasmon resonance, previously used to characterise the interaction between LdcI and RavA from *E. coli* (Snider et al., 2006; El Bakkouri et al., 2010), detected no interaction between *P. aeruginosa* LdcA and RavA (data not shown).

Cryo-EM Data Collection and 3D Reconstruction

For cryo-EM experiments, fresh LdcA was diluted in buffer containing 25mM Hepes, 0.1M NaCl, 0.1mM PLP, 1mM DTT, pH 7.5, to a final concentration of 0.4 mg/ml. 3 μl of sample were applied to glow-discharged quantifoil grids 300 mesh 1.2/1.3 (Quantifoil Micro Tools GmbH, Germany), excess solution was blotted with a Vitrobot (FEI) and the grid frozen in liquid ethane (Dubochet et al., 1988). Data collection was performed on a FEI Polara microscope operated at 300 kV under low dose conditions. Images were recorded on a K2 summit camera (Gatan, Inc., Pleasanton, CA) operated in a super-resolution mode with a pixel size of 0.815 Å. Movies of 40 frames were collected with an accumulated dose of 40 electrons/$Å^2$. Data collection and processing are summarized in Table S1. Beam induced motion correction was performed with RELION 3.0 (Zivanov et al., 2018) and estimation of CTF parameters was performed using Gctf (Zhang, 2016). Automatic particle picking was performed within RELION 3.0 using an initial low resolution LdcA map obtained from a

small subset of manually picked particles as a reference. Cleaning of selected LdcA particles was performed by reference-free 2D classification in RELION (Scheres and Chen, 2012). After 2D classification, iterative rounds of 3D refinement and 3D classification of the selected particles were performed followed by per particle CTF refinement and particle polishing as the final steps before post processing. A total of 66193 particles were used for the final cryo-EM reconstruction of 3.7 Å resolution as per the gold-standard FSC=0.143 criterion (Scheres and Chen, 2012). Local resolution was determined with ResMap (Kucukelbir et al., 2014).

Model Building, Refinement and Validation

A homology model of LdcA was obtained using the atomic coordinates of the AdcI (PDB ID 2VYC), exhibiting 40.76% identity with LdcA, as a template in Phyre2 (Kelley et al., 2015). The LdcA model was then fitted as a rigid body into the LdcA map using the fit-in-map module of UCSF Chimera (Pettersen et al., 2004). This rigid fit indicated movements of several parts of the protein. Therefore, the density corresponding to one LdcA monomer was extracted and flexible fitting was performed using IMODFIT (Lopéz-Blanco and Chacón, 2013) at 6 Å resolution. The structure obtained after IMODFIT was subjected to real space refinement applying secondary structure restraints in PHENIX (Adams et al., 2010). Iterative cycles of model building in COOT (Emsley and Cowtan, 2004) and model refinement using PHENIX were performed. The final model was validated using Molprobity (Chen et al., 2010). Model building statistics is summarized in Table S2. The FSC curve calculated between the final LdcA model and the map is shown Figure S2.

Isothermal Titration Calorimetry

All experiments were carried out using a MicroCal iTC200 instrument (Malvern) at 20°C. *E. coli* LdcI and *P. aeruginosa* LdcA were overproduced in Kan^R or Gm^R *E. coli* MG1655-derived strains respectively (i.e. MG1655 strains unable to synthetise ppGpp due to a Δ*rel*A Δ*spo*T mutation (Kanjee et al., 2011a) but producing the T7 polymerase and harboring either kanamicine or gentamicine resistance). The overexpressed proteins were purified by immobilized metal affinity chromatography (IMAC) using a Ni-NTA column, followed by a subsequent SEC step using a Sepharose-6 column. Final buffers after SEC were 25 mM HEPES, 0.3 M NaCl, 10% glycerol, 1 mM DDT, 0.1 mM PLP, pH 7.5 for LdcI, and 25 mM Tris-HCL, 0.3 M NaCl, 5% glycerol, 1mM DDT, 0.1 mM PLP, pH 7.5 for LdcA. Since PLP absorbs at 280 nm, final concentrations were measured using a Bradford Protein Assay (Bio-Rad) with BSA as a protein standard. To obtain the reaction enthalpy of the conversion of L-lysine to cadaverine by LdcI and LdcA, single injection mode (SIM) experiments were conducted using one injection of 40 μl 8 mM L-lysine over a period of 400 sec in 25 nM LdcI or 20 nM LdcA, followed by 1000 sec spacing. Used reaction buffers were 100 mM MES, 1 mM βME, 0.1 mM PLP, pH 6.5 and 100 mM Bicine, 1 mM βME, 0.1 mM PLP, pH 8.4 for LdcI and LdcA respectively. All following ITC experiments were conducted using 16 injections of 2.5 μl 8 mM L-lysine applied 100 sec. apart, in 2.5 nM LdcI or 2 nM LdcA, with and without the addition of 1 μM ppGpp in the sample cell. All experiments were performed in triplicate, and data was analyzed using the Michaelis-Menten kinetics module of the Origin ITC data analysis software to determine respective K_M, k_{cat} and k_I values.

Analysis of the *P. aeruginosa ravAviaA* Operon

The amino acid sequences of RavA (WP_005121444.1) and ViaA (YP_026243.1) from *E. coli* were used to detect homologues in the *Pseudomonas* database (www.pseudomonas.com; (Winsor et al., 2016)) by using BLASTP 2.2.6 (Altschul et al., 1997) using the BLOSUM45 matrix adapted for low identity percentages. Identification of *P. aeruginosa* strains presenting RavA and ViaA homologues was further refined by blasting the sequences of RavA (WP_003084152.1) and ViaA (WP_003084150.1) from the strain 39016 in the NCBI RefSeq Data Base, leading to the detection of MoxR AAA+ ATPase of 511 amino acids in 85 out of 4,129 analyzed *P. aeruginosa* strains. The *E. coli* RavA and its putative *P. aeruginosa* homologue share 32 % sequence identity and 48.4 % similarity. The AAA+ domain is more conserved than the triple helical domain and LARA domain. Secondary structure prediction and homology modeling with Phyre2 confirmed the presence of a triple helical domain in the *P. aeruginosa* homologue. Furthermore, a ViaA homologue of 499 amino acids was detected in the same strains and all identified *P. aeruginosa* ViaA homologues are 99 % identical, whereas they share 25.3 % identity and 41.5 % similarity with *E. coli* ViaA. Secondary structure predictions confirmed the presence of the distinctive VWA domain in the C-terminal part of the protein. Concerning the *ravA* and *viaA* genetic environment, we found that the 5'end of the ViaA coding region overlaps with the 3'end of the RavA coding sequence by 10 bases. This configuration is very similar to the 7 bases overlap of between the *ravA* and *viaA* coding regions of the *ravAviaA* operon in *E. coli*, suggesting that the operon arrangement is conserved in *P. aeruginosa*. The genetic environment of the *ravAviaA* operon in the identified strains was analyzed with the GeneSpy software (http://lbbe.univ-lyon1.fr/GeneSpy/index.html). We performed an HmmScan to seek for the presence of homologous domains and identify the proteins encoded by the genomic islands identified with Genespy. Pfams were used to confirm the presence of defense island gene homologues published in (Doron et al., 2018).

Phylogeny: Dataset Assembly

Functionally characterized sequences of AAT-fold LAOdcs were retrieved from NCBI: LdcI (NP_418555.1), LdcC (NP_414728.1), AdcI (NP_418541.1), OdcC (NP_417440.1), and OdcI (NP_415220.1) from *E. coli* str. K-12 substr. MG1655 and LdcA (NP_250509.1) from *P. aeruginosa* PAO1. These sequences were used as seeds to query a local database containing 4,466 complete proteomes of prokaryotes downloaded from the NCBI (ftp://ftp.ncbi.nlm.nih.gov) with the BLASTP 2.2.6 software (Altschul et al., 1997) using default parameters. Homologues of LAOdc were retrieved and aligned using MAFFT v7 (Katoh and Standley, 2013). The resulting multiple alignment was used to build a HMM profile with the HMMbuild program from the HMMER v3.1b1 package (McClure et al., 1996). This profile was then used to query the local database of complete proteomes with the HMMsearch program.

Sequences with e-values lower than 2.2e-13 were retrieved. Finally, the search for potential unannotated sequences was performed using TBLASTN 2.2.6 on genomic sequences corresponding to the 4,466 complete proteomes. This led to the identification of 4,090 homologous sequences, among which 418, 395, 872, and 1,010 correspond to AdcI, LdcA, LdcIC and OdcIC, respectively.

Phylogeny: Phylogenetic Inference

For phylogenetic inference we sampled 34 sequences representative of the genetic and taxonomic diversity of AdcI, LdcA, LdcIC and OdcIC. A multiple alignment was built with MAFFT using the L-INS-i option that allows the construction of accurate alignments and trimmed with BMGE v1.1 with matrix substitution BLOSUM30 (Criscuolo and Gribaldo, 2010). For phylogenetic analyses, OdcIC sequences were used as outgroup, in agreement with our previous study. A maximum likelihood tree was inferred with PhyML 3.1 (Guindon et al., 2010). The best suited evolutionary model was selected using the model test tool implemented in IQ-TREE v1.4.1 according to the BIC criteria (Nguyen et al., 2015). The robustness of the inferred tree was assessed using the non-parametric procedure implemented in PhyML (100 replicates of the original dataset). Alignments have been visualized using aliview 1.21 (Larsson, 2014). Figures of trees have been generated using iTOL (Letunic and Bork, 2016) and seaview 4.6.4 (Gouy et al., 2010).

Phylogeny: Sliding Window Approach

A sliding window of 80 amino-acids was moved all along the multiple alignment with a sliding step of 5 amino-acids. For each of the 157 windows, a ML tree was inferred using PhyML (LG+I+G4 model). The robustness of the inferred trees was assessed using the non-parametric procedure implemented in PhyML (100 replicates of the original dataset). A phylogenetic network was inferred with SplitTree 4 (Huson and Bryant, 2006) to visualize the topological consistency of the 157 ML trees. To analyse the phylogenetic signal contained in the sequences, we used the ete3 API library (Huerta-Cepas et al., 2016). LdcA sequences from *Pseudomonadaceae* and *Betaproteobacteria* did not group together in 49 trees (32%). The monophyly of the AdcI subfamily was recovered in 80 trees only. Last but not least, the four subfamilies were connected through a reticulated network, underlying again major inconsistencies among ML trees.

The SubMLT and SubBRT scores focused on the monophyly of the LAOdc subfamilies. (i) The SubMLT score is computed for each sliding window and for each subfamily. It is set to 1 if the considered subfamily is monophyletic in the ML tree, otherwise 0. (ii) The SubBRT score is computed for each sliding window and for each subfamily. It corresponds to the bootstrap value supporting the monophyly of the considered subfamily. The RelMLT, RelBRT and CumRelMLT scores described the relationships among subfamilies. Because four subfamilies are considered, three possible relationships are expected: the grouping of LdcA with AdcI, the clustering of LdcA with LdcIC, and the sistership of LdcIC and AdcI. (i) The RelMLT score is computed for each sliding window and for each of the three possible relationships among subfamilies. It is set to 1 if the considered relationship among two subfamilies is observed in the ML tree, otherwise 0. (ii) The RelBRT score is computed for each sliding window and for each of the three possible relationships among subfamilies. It corresponds to the bootstrap value supporting a given relationship among subfamilies. (iii) The CumRelMLT score is computed for each amino acid position of the multiple alignment as the sum of RelMLT scores associated to sliding windows containing the considered amino acid position. CumRelMLT values have been mapped on LdcI structure using a color gradient to correlate phylogenetic signal with structural information.

Galleria mellonella Treatment Assays

G. mellonella larvae (greater wax moth) were obtained from TrueLarv UK Ltd. (Exeter, UK) and stored at 15°C prior to use. The virulence of three strains - the wild-type reference strain PAO1, the mutant deleted of the *ldcA* gene (PAO1 *ΔldcA*) and the complemented strain PAO1 *ΔldcA::ldcA,* constructed and initially characterized in (Carriel et al., 2018) - was assessed as described previously (Desbois and Coote, 2011), except for the following differences. *P. aeruginosa* strains were grown exponentially for 2 hours, washed with PBS buffer and adjusted to an OD_{600} of 0.1. The strains were further diluted with PBS and plated to determine the CFU of the inoculation suspension. Larvae were inoculated with 10 µl of a 2.5×10^3 CFU/mL solution and incubated at 37°C. In total 25 larvae were used per condition, split in 3 independent experiments. Mock-inoculated (sterile PBS) animals were used as controls. Survival of a larva was determined by the ability to respond to external stimuli (poking). Statistical analysis was performed using the log rank test (Bland and Altman, 1986) and p-values were corrected using the Benjamini-Hochberg method (Benjamini and Hochberg, 1995). Pairwise difference p-values are as follows: PAO1 versus PAO1 *ΔldcA*: 2.6×10^{-5}; PAO1 versus PAO1 *ΔldcA::ldcA* 0.0820 and PAO1 *ΔldcA* versus PAO1 *ΔldcA::ldcA* 0.0023.

QUANTIFICATION AND STATISTICAL ANALYSIS

Cryo-EM refinement statistics and validation statistics are presented in Table S1. Quantification and statistical details of the ITC analysis are summarised in Figure S4 legend and in the corresponding Method Details section. Quantification and statistical details of the *G. mellonella* survival assays are presented in the Figure 6 legend and in the corresponding Method Details section.

DATA AND CODE AVAILABILITY

Cryo-EM map of LdcA and the corresponding atomic model have been deposited to the EMDB and PDB with accession codes EMD-4468 and PDB-6Q6I.

Structure, Volume *27*

Supplemental Information

Structure, Function, and Evolution of the *Pseudomonas aeruginosa* Lysine Decarboxylase LdcA

Eaazhisai Kandiah, Diego Carriel, Pierre Simon Garcia, Jan Felix, Manuel Banzhaf, George Kritikos, Maria Bacia-Verloop, Céline Brochier-Armanet, Sylvie Elsen, and Irina Gutsche

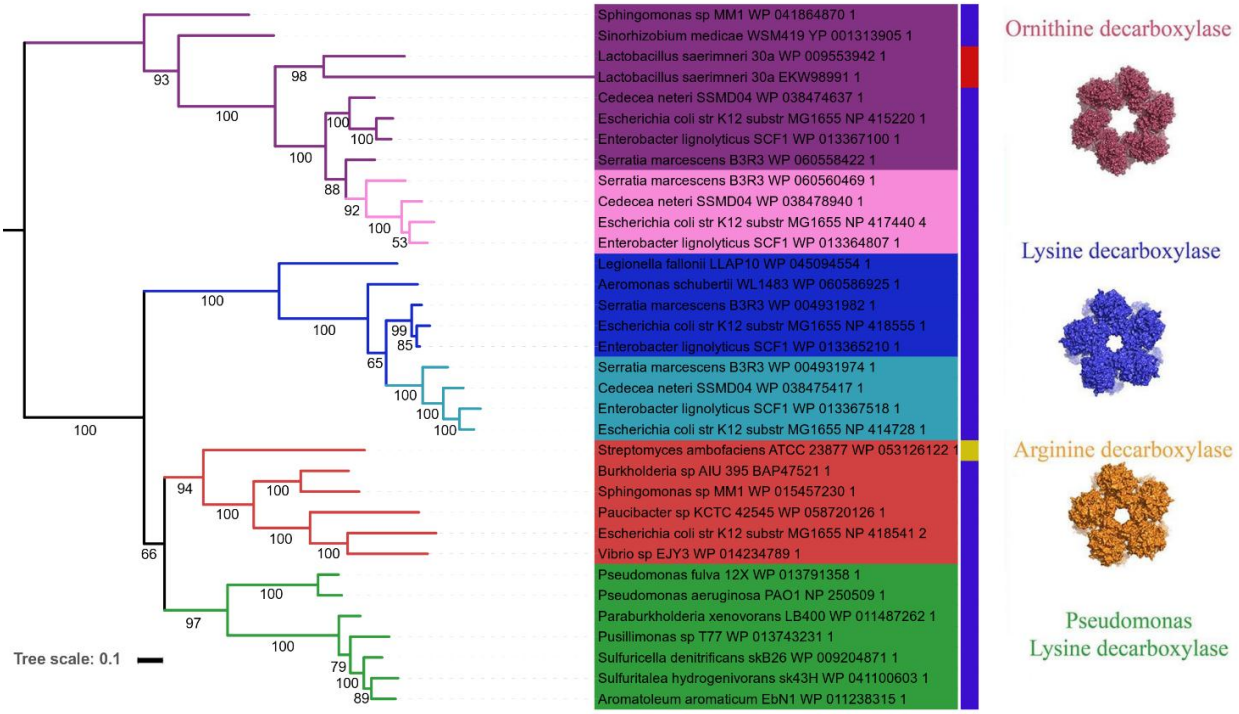

Figure S1, related to Figure 1: Evolution of proteobacterial LOAdcs.

Maximum likelihood tree of proteobacterial LAOdc (34 sequences, 638 amino acid positions). Color of leaves correspond to subfamilies (OdcI : violet, OdcC: pink, LdcI: blue, LdcC: turquoise, AdcI: red, LdcA: green). Color of strip correspond to taxonomy (Proteobacteria: blue, Firmicutes: red, Actinobacteria: yellow). Bootstrap values are indicated on branches. The scale bar is proportional to the average number of substitution per site. Available 3D structures of representative of each subfamily are shown on the right-hand side: OdcI (PDB 1ORD), LdcI and LdcC (PDB 3N75 for LdcI) and AdcI (PDB 2VYC).

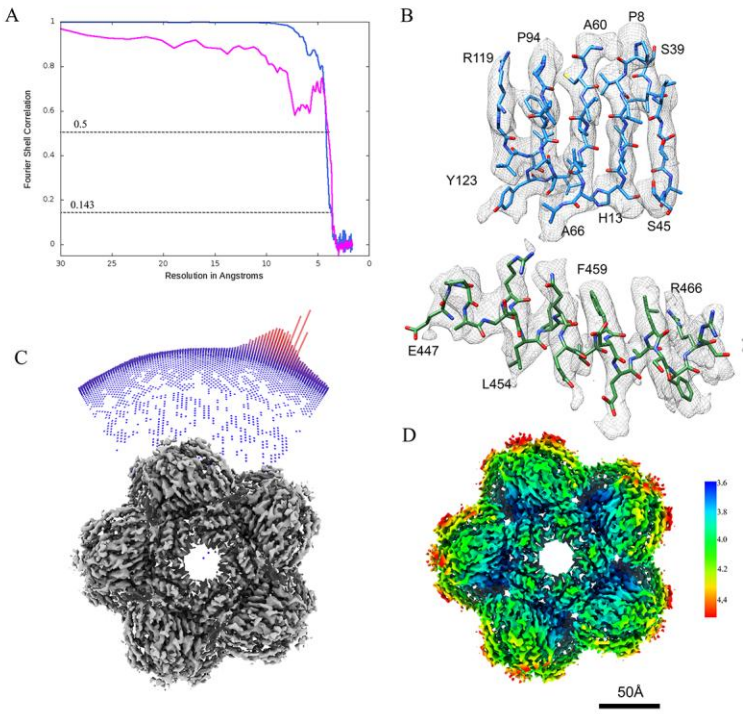

Figure S2, related to Figure 1: LdcA cryo-EM map and validation.

(A) FSC curves of the LdcA map. Corrected FSC of the masked map is shown in blue, FSC curve of the map versus the model in pink. (B) Representative regions illustrating the densities and the quality of the model. (C) Distribution of Euler angles. (D) Local resolution mapped onto the cryo-EM density.

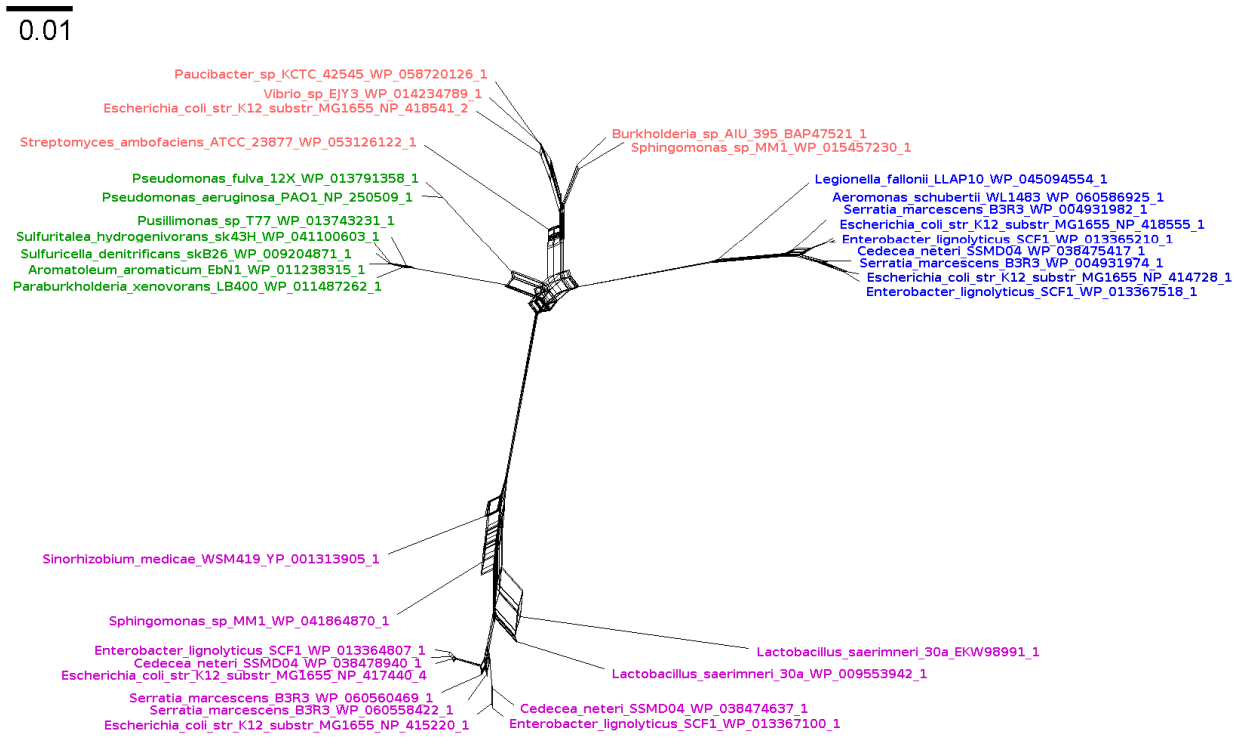

Figure S3, related to Figure 3: Phylogenetic network of LAOdc sequences from sliding windows alignments.

This network has been inferred with the 157 ML trees associated to sliding window approach. Each edge corresponds to an alternative topology. Red: AdcI, green: LdcA, blue: LdcIC, violet: OdcIC. Scale bar corresponds to the number of substitutions per site.

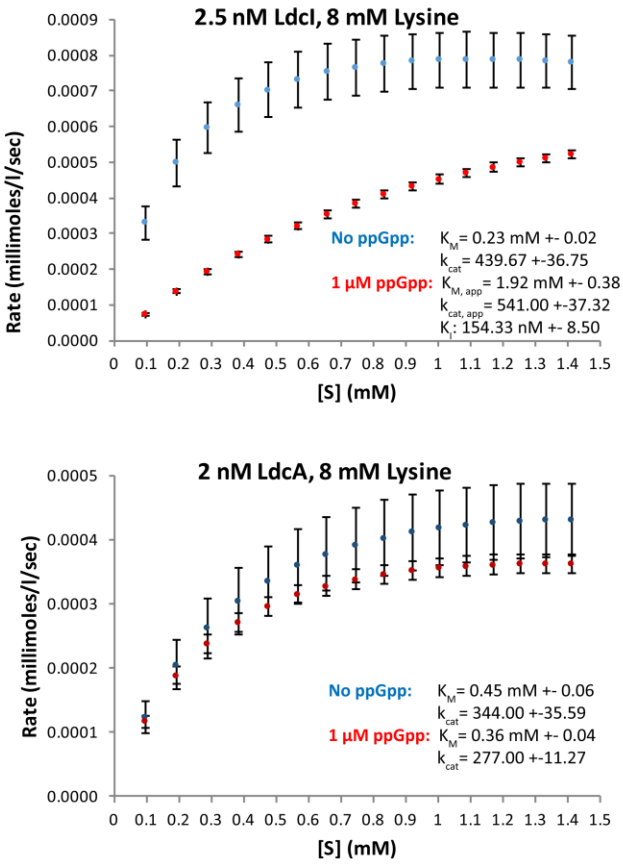

Figure S4, related to STAR Methods: Kinetics of LdcI and LdcA lysine decarboxylase activity in the presence or absence of ppGpp, determined by Isothermal Titration Calorimetry.

Blue curves display lysine decarboxylase activity in the absence of ppGpp for LdcI (top) and LdcA (bottom), while red curves show the activity upon addition of 1 µM ppGpp. Error bars represent the standard deviation (s.d.) calculated from the measurements of three replicate experiments. Calculated K_M, k_{cat} and K_I values (app = apparent) for LdcI/LdcA activity in the presence or absence of ppGpp are shown.

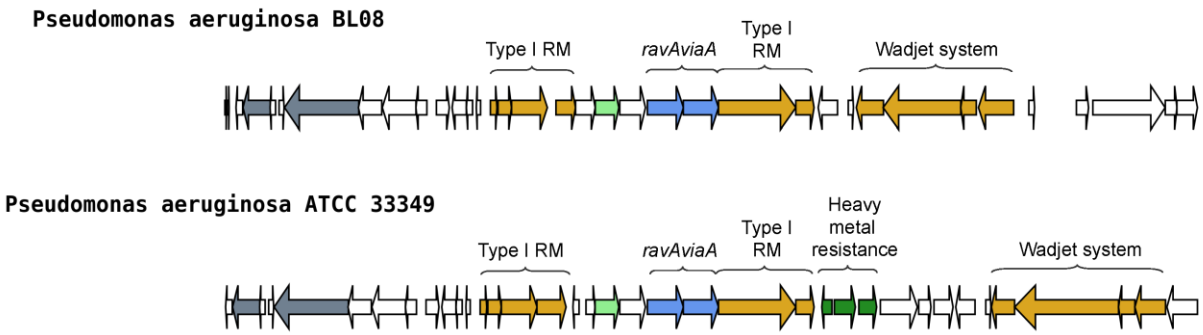

Figure S5, related to STAR Methods: Genomic islands containing *ravA* and *viaA*.
Genomic island (A) is present in most *P. aeruginosa* strains and contains genes involved in DNA mobility such as integrases, in defense against phages (Type I RM, CRISPR-Cas2) and foreign plasmids (Type I Wadjet) and toxin-antitoxin systems. Genomic island (B) appears as a modified version of (A) in which other genes involved in heavy metal resistance are present as well as an analog Type I Wadjet system. Both elements are found integrated at a tRNAArg gene. HMMSCAN (EMBL-EBI) was used to predict gene function (highest E-value score). Genes predicted to be involved in mobility are in gray, defense systems are in yellow, toxin-antitoxin systems are in pale green, heavy metal resistance genes are in green, *ravAviaA* operon is in blue.

Data-Collection and Refinement Statistics	
Microscope	POLARA
Camera	K2
data collection mode	super-resolution
Defocus-range (um)	0.9 – 2.9
Voltage (kV)	300
Electron dose (e^{-}/Å^{-2})	40
Pixel size (Å)	0.815
Final number of Particles	6619
Resolution estimate (Å)	3.7
Model building Statistics	
Total residues	7490
Number of chains	10
Ramachandran outliers	0.27 %
Favored	83.15 %
Rotamer outliers	1.7 %
Clashscore	8.4
MolProbity score	2.65

Table S1, related to Figure 1: Cryo-EM data collection, refinement statistics and validation statistics.

		decamer	monomer	Wing	Core	PLP binding domain	ppGpp binding domain	CTD
LdcA	OdcI*	3.1	2.7	4.7	2.3	2.2	2.9	2.4
	AdcI	2.9	2.5	2.7	2.0	1.6	2.0	2.4
	LdcI	3.5	2.4	3.3	2.0	1.7	2.2	2.0

Table S2, related to Figures 2, 4 and 5: RMSD-based comparison between LdcA, LdcI, AdcI and OdcI structures.

* RMSD was calculated for OdcI dimer against LdcA dimer.

PLP binding site				
		CumRelMLT values		
LdcA	LdcI	LdcA(AdcI,LdcIC)	AdcI(LdcIC,LdcA)	LdcIC(LdcA,AdcI)
T239	T220	12	0	4
S240	S221	12	0	4
H264	H245	9	1	6
A355	D330	1	6	0
A357	A332	1	7	0
W358	W333	1	7	0
S390	S364	1	14	0
H392	H366	1	14	0
K393	K367	1	15	0
T429	T399	0	14	2
S430	S400	0	14	2

ppGpp binding pocket				
		CumRelMLT values		
LdcA	LdcI	LdcA(AdcI,LdcIC)	AdcI(LdcA,LdcIC)	LdcIC(LdcA,AdcI)
R119	R97	12	1	2
R225	R206	15	0	1
E447	K417	0	11	5
G448	G418	0	10	6
R595	R558	0	3	13
P602	R565	0	2	14
D605	N568	0	1	15
G622	R585	0	0	15

Table S3, related to Figure 5: Relevant LdcA and LdcI residues in the active site and in the ppGpp binding pocket with CumRelMLT values for the three possible topologies as used to make the Figure 5.

	Monomer-monomer in dimer	Monomer-monomer in pentamer
OdcI	6068	743
AdcI	5328	1192
LdcI	11000	1204
LdcA	5587	1116

Table S4, related to Figure 4: Interface area in LdcA, LdcI, AdcI and OdcI structures, Å^2.